Research Square

Preprints are preliminary reports that have not undergone peer review.
They should not be considered conclusive, used to inform clinical practice,
or referenced by the media as validated information.

Background simulation and design optimization of a balloon-borne TES spectrometer for 511-keV observations

Haoyu Li
Key Laboratory of Particle Astrophysics, Institute of High Energy Physics, Chinese Academy of Sciences
Daikang Yan
yandk@ihep.ac.cn
Key Laboratory of Particle Astrophysics, Institute of High Energy Physics, Chinese Academy of Sciences
Hua Feng
Key Laboratory of Particle Astrophysics, Institute of High Energy Physics, Chinese Academy of Sciences
He Gao
Key Laboratory of Particle Astrophysics, Institute of High Energy Physics, Chinese Academy of Sciences
Dongya Guo
Key Laboratory of Particle Astrophysics, Institute of High Energy Physics, Chinese Academy of Sciences
Jiangzhen Hong
Nanchang University
Weichun Jiang
Key Laboratory of Particle Astrophysics, Institute of High Energy Physics, Chinese Academy of Sciences
Ming Li
Institute of High Energy Physics
Zhengwei Li
Key Laboratory of Particle Astrophysics, Institute of High Energy Physics, Chinese Academy of Sciences
Congzhan Liu
Key Laboratory of Particle Astrophysics, Institute of High Energy Physics, Chinese Academy of Sciences
Wenxi Peng

Key Laboratory of Particle Astrophysics, Institute of High Energy Physics, Chinese Academy of Sciences

Jia Quan
Technical Institute of Physics and Chemistry

Xilu Wang
Key Laboratory of Particle Astrophysics, Institute of High Energy Physics, Chinese Academy of Sciences

Lingjiao Wei
Technical Institute of Physics and Chemistry

Yifei Zhang
Key Laboratory of Particle Astrophysics, Institute of High Energy Physics, Chinese Academy of Sciences

Jianghua Zhou
Aerospace Information Research Institute

Rongchen Zhu
Aerospace Information Research Institute

Research Article

Keywords: Galactic center, 511 keV annihilation, transition-edge sensor, activation background

Posted Date: November 24th, 2026

DOI: https://doi.org/10.21203/rs.3.rs-11698046/v1

License: This work is licensed under a Creative Commons Attribution 4.0 International License.
Read Full License

Additional Declarations: No competing interests reported.

Background simulation and design optimization of a balloon-borne TES spectrometer for 511-keV observations

Haoyu Li[1,2,4], Daikang Yan[1,2,4,*], Hua Feng[1,2,4], He Gao[1,2,4], Dongya Guo[1,2,4,*], Jiangzhen Hong[3], Weichun Jiang[1,2,4], Ming Li[2,4], Zhengwei Li[1,2,4], Congzhan Liu[1,2,4], Wenxi Peng[1,2,4,*], Jia Quan[2,5], Xilu Wang[1,2,4,*], Lingjiao Wei[2,5], Yifei Zhang[1,2,4], Jianghua Zhou[2,6], Rongchen Zhu[2,6]

[1]Key Laboratory of Particle Astrophysics, Institute of High Energy Physics, Chinese Academy of Sciences, Beijing 100049, China
[2]University of Chinese Academy of Sciences, Beijing 100049, China
[3]School of Physics and Materials Science, Nanchang University, Nanchang 330031, China
[4]Institute of High Energy Physics, Chinese Academy of Sciences, Beijing 100049, China
[5]Technical Institute of Physics and Chemistry, Chinese Academy of Sciences, Beijing 100190, China
[6]Aerospace Information Research Institute, Chinese Academy of Sciences, Beijing 100094, China

Corresponding authors: [*]yandk@ihep.ac.cn (Daikang Yan)
[*]guody@ihep.ac.cn (Dongya Guo)
[*]pengwx@ihep.ac.cn (Wenxi Peng)
[*]wangxl@ihep.ac.cn (Xilu Wang)

Abstract Balloon-borne focusing spectrometers that combine a Laue lens with transition-edge sensor (TES) microcalorimeter arrays offer sub-keV spectral resolution for pointed observations of the Galactic center 511 keV positron annihilation line, while their sensitivity is strongly constrained by the cosmic-ray-induced background in the stratosphere. In this work, we simulate the cosmic background of a balloon-borne TES spectrometer coupled to a Laue lens using Geant4 and MEGAlib, evaluate the spectrometer's performance, and compare two cryostat configurations to improve its sensitivity. Focused signal photons, prompt atmospheric backgrounds, and delayed activation decays are processed using consistent detector-response and event-selection methods. The calculation assumes an on-axis monochromatic 511-keV source, a single-pixel energy resolution of 500 eV full width at half maximum, and a 510.50–511.50 keV analysis window. In the typical Under-stage configuration, where the TES array is mounted directly beneath the dilution-refrigerator cold stages, copper contributes 59.5% of the selected day-15 delayed background. This finding motivates the evaluation of an alternative Lateral-chimney configuration. For an idealized 20-day on-source observation including time-dependent activation and atmospheric transmission, the projected top-of-atmosphere 3σ minimum detectable line flux for the Lateral-chimney configuration is $(3.30 \pm 0.28) \times 10^{-5}\,\mathrm{ph\,cm^{-2}\,s^{-1}}$, a factor of 2.10 below that of the Under-stage configuration. Nearby copper supports and the heat-sink ring remain the main targets for further background reduction.

Keywords Galactic center, 511 keV annihilation, transition-edge sensor, activation background

1 Introduction

Galactic 511 keV annihilation radiation is a key observational probe of the production, propagation, and annihilation environments of Galactic positrons. Its spectrum contains a two-photon line near 511 keV and an ortho-positronium continuum at lower energies. Positrons annihilate directly with electrons or form para-positronium, producing two photons near 511 keV, whereas ortho-positronium decays into a three-photon continuum. The line intensity, profile, and positronium continuum therefore constrain the medium in which positrons slow down and annihilate [1, 2]. Under an approximate steady-state assumption, the total Galactic 511 keV flux measured by INTEGRAL/SPI corresponds to an annihilation rate of a few $\times 10^{43}\,\mathrm{e^{+}\,s^{-1}}$ [1, 3]. Proposed positron sources include β^{+}-unstable nuclei synthesized in stellar explosions, compact objects capable of producing electron–positron pairs, and more speculative particle-physics scenarios in which annihilating or decaying light dark matter injects low-energy positrons. Existing observations do not uniquely determine the dominant contribution [1, 4, 5].

Wide-field observations have established the diffuse morphology of the line. INTEGRAL/SPI finds a bright central bulge and a weaker disk, and a recent 20-year analysis recovers central, broad-bulge, and disk components while the evidence for additional correlated structures remains marginal [4, 6, 7]. The 2016 COSI balloon flight independently

detected the bulge and found evidence that the emission is more extended than a single point source [3, 8]. Spectroscopy also constrains the annihilation medium and kinematics: the SPI spectrum can be decomposed into a narrow component with about $1.3\,\mathrm{keV}$ FWHM and a broad component with about $5.4\,\mathrm{keV}$ FWHM, and spatial variations in centroid energy and width have been sought across the inner Galaxy [2, 9]. The annihilation map, however, records where positrons slow down and annihilate, not necessarily where they were created. Propagation through a magnetized, multiphase interstellar medium means that diffuse morphology and spectroscopy alone cannot recover the dominant source class or the complete pre-annihilation transport history [1].

Wide-field Compton and coded-mask instruments are well suited to the total bulge and disk emission. A complementary pointed instrument is needed to test whether the central region also contains an unresolved central enhancement, compact sources, or measurable line-kinematic structure. A detection of a point-like or narrowly concentrated feature would show that part of the annihilation is spatially localized; a non-detection would constrain a compact component without excluding source populations whose positrons escape and annihilate diffusely. An INTEGRAL/IBIS point-source search found no Galactic 511 keV point sources and set a 2σ upper limit of about $1.6 \times 10^{-4}\,\mathrm{ph\,cm^{-2}\,s^{-1}}$ for a ~ 10 Ms Galactic-center exposure [10]. This limit provides a benchmark for a narrow-field pointing instrument.

Laue optics use transmission-mode Bragg diffraction to focus photons arriving from a known direction onto a compact focal plane [11, 12]. When detector-related background dominates, concentrating photons collected over a large aperture onto a small sensitive detector area improves point-source sensitivity [13]. The focal-plane detector must combine high energy resolution with sufficient stopping efficiency at 511 keV. Transition-edge-sensor (TES) microcalorimeters measure the small temperature rise produced by deposited energy through the steep resistive transition of a superconductor and are projected to achieve sub-keV energy resolution at 511 keV [14]. An array covers the focal spot, while thick absorbers and a multilayer layout increase the full-energy-peak efficiency. The resulting narrow-field focusing spectrometer trades sky coverage for a concentrated source beam and high-resolution spectroscopy. Building on previous wide-field measurements of the Galactic bulge and disk, it supports dedicated searches for point sources. The Laue-lens energy acceptance determines which photons are focused, the TES energy resolution sets the instrumental contribution to the measured line width, and the analysis energy window selects events used in the background and sensitivity calculation.

The 511-CAM concept proposed by Shirazi et al. [14] combines gamma-ray optics with stacked TES arrays for pointed 511 keV observations. Their mission study simulated the response of a detector array enclosed by active BGO shielding, adopted the Gehrels shield-leakage background model to estimate sensitivity, and estimated the overall background rate by scaling XL-Calibur balloon-flight measurements according to detector mass. Hu et al. [15] subsequently described the collimated 511-Spectrometer Mission, reported tests of TES prototypes with thick Bi absorbers, and estimated its flight sensitivity using an empirical scaling of background rates measured during the 2022 XL-Calibur balloon flight. Monte Carlo simulations based on detailed instrument mass models are also commonly used to evaluate instrument backgrounds in similar high-energy astronomy missions and can further resolve the contributions of individual mechanical and cryogenic components to the instrument background [16, 17].

This work uses Monte Carlo simulations to quantify the prompt and delayed activation backgrounds of a balloon-borne spectrometer. The spectrometer uses a Laue lens for high angular resolution and a six-layer TES array for high energy resolution. The instrument mass model includes mainly the dilution refrigerator and scintillator crystals. The simulation accounts for radionuclide buildup and decay, as well as variations in the signal and background with flight time and trajectory. The effects of scintillator-based active anticoincidence, event selection based on multipixel topology, and Compton kinematics on signal retention and background suppression are also evaluated. The selected background is traced to its incident particles, materials, parent nuclides, and production components to identify the dominant background sources. Two cryostat configurations are then compared to quantify how changes in TES-array position and active-shield coverage affect the 511 keV background and point-source sensitivity.

Sections 2–4 define the mass models and simulation framework and compare their balloon background and point-source sensitivity. Section 5 estimates the response for Antarctic balloon flights, LEO, the lunar surface, and Sun–Earth L2; Sections 6 and 7 summarize the design implications and next steps, respectively.

2 Detector and cryostat mass model

The Under-stage reference configuration contains a six-layer TES array and a compact dilution refrigerator (DR) with a mixing chamber (MC), staged cold plates, thermal and magnetic shields, copper supports, active scintillators, and cryogenic service structures [14, 18].

The TES detector concept uses an AlMn TES developed in our laboratory. The transition temperature of AlMn can be tuned through its composition and annealing process [19]. AlMn films can be deposited and patterned for TES-array fabrication [20]; they also have relatively low magnetic-field sensitivity [21]. In the present conceptual design, the AlMn TES is an approximately $200\,\mathrm{nm}$-thick film with an Mn doping concentration of $2000\,\mathrm{ppm}$ on an atomic basis, whereas the γ-ray absorber is a millimeter-scale metal body.

Each pixel has one Ta absorber measuring $1.5 \times 1.5 \times 3.0\,\mathrm{mm}^3$. Ta is a high-atomic-number material with substantial interaction probability for 511 keV photons. At 511 keV, a single $3.0\,\mathrm{mm}$ Ta layer has an estimated interaction efficiency of about 48%, and the corresponding six-layer interaction probability is about 98% [22]. In the current geometry, adjacent Ta

array layers have a center-to-center spacing of $12\,\mathrm{mm}$; this spacing was chosen with a subsequent veto based on Compton-kinematic event reconstruction in mind. Ta was also selected for its low superconducting specific heat in the cryogenic regime ($5.99 \times 10^{-7}\,\mathrm{J\,kg^{-1}\,K^{-1}}$ at $100\,\mathrm{mK}$ [23]). Ta also has a relatively high photoelectric-to-Compton interaction ratio. From tabulated photon-interaction cross sections near 511 keV, this ratio is approximately 0.793 [22]. The expected detector energy resolution is $\Delta E_{\mathrm{FWHM}} = 500\,\mathrm{eV}$ at 511 keV, which is used as the detector-response post-processing input.

The focal-plane array comprises six layers, each containing 376 Ta absorber pixels, for a total of 2256 pixels. In the pixel concept shown in Figure 1(a), the Ta absorber is thermally coupled to the AlMn TES, with an Nb electrical lead. A suspended $\mathrm{Si_3N_4}$ membrane supports this structure and provides the weak thermal link to the Si frame.

Figure 1(b) illustrates the electrothermal operating principle. Energy deposited in the absorber raises the temperature and resistance of the TES. Under approximately constant voltage bias, the TES current falls, producing a pulse measured by a superconducting quantum interference device (SQUID). The accompanying reduction in Joule heating provides negative electrothermal feedback, while the membrane conducts heat to the bath [18].

Because the TES film and Ta absorber differ greatly in dimensions and mass, and because the TES film itself contributes negligibly to interactions at 511 keV, the transport geometry uses the Ta absorber as the principal sensitive volume of each TES pixel. A simplified Si-substrate model is placed below each Ta pixel to represent the substrate and support mass. The thin-film thermal link, TES film, wiring, and readout details are not constructed layer by layer as explicit interaction volumes, but enter the model through the assumed energy response and simplified models of ancillary components.

Figure 2 shows the reference cryostat and focal-plane arrangement. Bismuth germanate (BGO) shielding and the mechanical enclosure surround the dilution refrigerator, leaving openings for the gas lines.

The DR provides an ultra-low-temperature environment of approximately $100\,\mathrm{mK}$ for the TES. It offers continuous cooling, low electromagnetic interference, and low vibration. As shown in Figure 2, the four cold plates correspond to the $60\,\mathrm{K}$, $4\,\mathrm{K}$, still ($1\,\mathrm{K}$), and MC ($0.1\,\mathrm{K}$) stages. The TES array is located below the MC cold plate and is thermally connected to it via high-purity oxygen-free copper thermal straps.

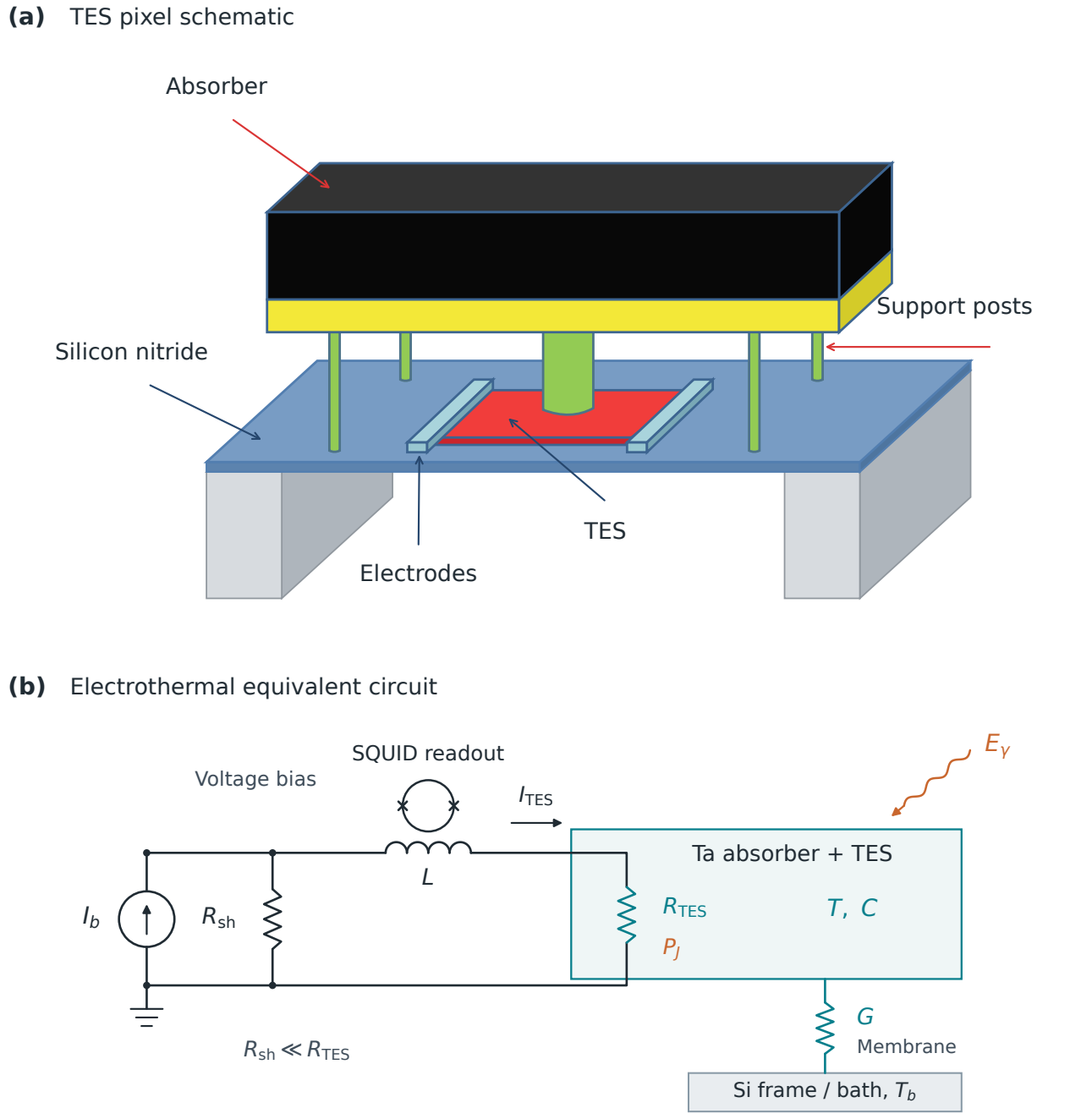

Fig. 1 TES pixel concept and operating principle. (a) A Ta absorber is thermally coupled to an approximately 200 nm AlMn TES, with an Nb lead. The suspended Si_3N_4 membrane provides the weak thermal link to the Si frame; film thicknesses are enlarged for clarity. (b) Simplified electrothermal circuit: the absorber and TES have total heat capacity C at temperature T, with thermal conductance G to the bath at T_b. A bias current I_b and shunt resistor $R_{\rm sh} \ll R_{\rm TES}$ provide approximate voltage bias. The TES branch carries current $I_{\rm TES}$ through inductance L and is coupled to the SQUID readout; P_J denotes Joule heating

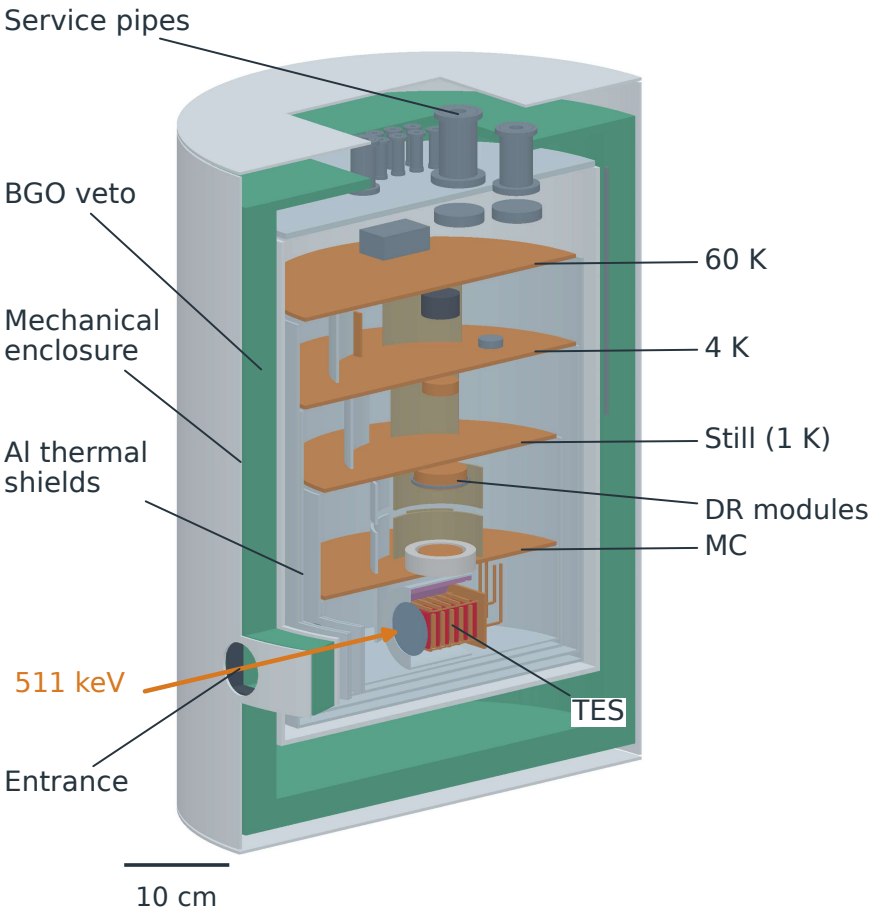

Fig. 2 Orthographic cutaway of the Under-stage reference configuration, showing the cold plates, DR components, service pipes, TES, Al cryostat and thermal shields, and BGO. Sectors of the shells, covers and plates are removed to expose the interior, retaining the complete entrance rims. The orange arrow indicates the focused 511 keV beam. Dense hole arrays in the cold plates are omitted for clarity

3 Simulation framework

Detector-side particle transport was performed with Cosima in MEGAlib 4.02.00 (Geant4 10.02.p03), using the `LivermorePol` electromagnetic and `qgsp-bic-hp` hadronic physics lists [24–26]. Cosima defines sources and detector geometry, transports particles through the mass model, and records interactions for detector-response and event-selection analysis. A uniform production range cut of $5\,\mu\mathrm{m}$ was used for detector-side transport. Figure 3 summarizes the end-to-end calculation in three physical branches: focused signal, prompt atmospheric background, and delayed activation background. The Laue optics and the detector–cryostat system were represented by separate mass models. The reference point source was first transported through the Laue-lens model; the positions and directions of photons reaching the focal plane were written to a MEGAlib EventList and used to initialize detector-side Monte Carlo transport. The focused signal and all backgrounds were transported through each detector–cryostat mass model.

Prompt transport and activation-production transport were run in parallel from the same EXPACS/PARMA atmospheric field for eight particle species: γ, e^-, e^+, μ^-, μ^+, n, p, and α. In the delayed-activation branch, BUILDUP transport recorded nuclide yields, material volumes, and production positions. These records were used to calculate the activity accumulated during the flight and to construct the radionuclide inventory at each reference epoch; delayed decays were then sampled at the recorded production positions and transported through the detector–cryostat model.

The focused signal, eight prompt species, and delayed activation use the same detector response within each model. The analysis-window cut is followed by the geometry-specific active veto and common Compton event selection. Selected backgrounds are decomposed by incident particle, parent nuclide, material, and production volume before the mission-time integration. The subsections below define the source models, transport normalization, event selection, and mission-time calculation.

3.1 Laue optics and detector-coupled signal transport

The Laue lens uses mosaic Ge(111) crystals [11, 12]. The reference design focuses an on-axis monochromatic $511\,\mathrm{keV}$ source at a distance of 10 m. It consists of 25 crystals on a ring of radius 74.28 mm, each with a thickness of 10.22 mm and an $18 \times 18\,\mathrm{mm}^2$ radial–tangential envelope. The two inner corners of each tile are clipped to its allocated angular sector, with an assumed 0.2 mm gap between neighboring sectors. This non-overlapping arrangement has a total projected crystal area of $A_{\mathrm{inc}} = 79.56\,\mathrm{cm}^2$.

Diffraction is implemented as a user-defined discrete physics process in Geant4 11.4.0 [25, 26], using the ideally imperfect mosaic approximation [27]. The separate optical model uses `G4EmStandardPhysics` with a $0.1\,\mathrm{mm}$ production range cut. The local scattering coefficient $\sigma(\mathbf{u})$ depends on the photon propagation direction $\mathbf{u}$ and gives the mean free path $\lambda_{\mathrm{diff}}(\mathbf{u}) = 1/\sigma(\mathbf{u})$. Geant4 samples this process in competition with photoelectric absorption, Compton scattering, and Rayleigh scattering. Repeated diffraction, including transfer back toward the transmitted beam, is allowed on the same photon track; the interaction optical depth is resampled after each diffraction.

The scattering coefficient is normalized using XOP/CRYSTAL reference rocking curves [28], with Ge anomalous scattering factors evaluated by xraylib 4.2.1 [29] at $511\,\mathrm{keV}$, $d_{111} = 3.2666$ Å, and a unit temperature factor. For each polarization, the local coefficient is extracted from the two-beam relation for a symmetric reference slab,

$$R_{\mathrm{ref}}(L) = \frac{1 - \exp(-2\sigma L)}{2} \exp(-\mu_{\mathrm{ref}} L), \tag{1}$$

where R_{ref} is the slab diffraction probability, L is the full path through the reference slab, and μ_{ref} is the photoelectric attenuation coefficient used by XOP. The two polarization coefficients are averaged for the unpolarized source. The extracted σ was insensitive to the reference slab thickness over the range tested. Reference attenuation is removed when extracting σ; electromagnetic interactions in the transport calculation are supplied by Geant4.

The microcrystallite orientations follow a narrow Mises–Fisher distribution with an adopted 30 arcsec FWHM [27], corresponding in the narrow-angle limit to $\sigma_{\mathrm{mos}} = 30\ \mathrm{arcsec}/\sqrt{8\ln 2}$. Given the incident direction and energy, the microcrystallite normal $\mathbf{n}$ is sampled from this distribution conditionally on the Bragg constraint [30],

$$\mathbf{u} \cdot \mathbf{n} = \sin\theta_B, \qquad \mathbf{u}' = \mathbf{u} - 2(\mathbf{u} \cdot \mathbf{n})\mathbf{n}. \tag{2}$$

Here θ_B is the Bragg angle and $\mathbf{u}'$ is the outgoing direction. Diffraction conserves photon energy. The custom process treats the selected $\pm(111)$ reflection at $511\,\mathrm{keV}$; photons shifted away from this energy continue under standard electromagnetic transport. The calculation assumes ideally aligned, ideally imperfect mosaic crystals and neglects primary extinction within finite microcrystallites.

Single-crystal tests spanning 1–20 mm in thickness and angular offsets up to ± 60 arcsec agreed with two-beam predictions for the diffracted, transmitted, and uncollided fractions. We checked the scattering normalization against the structure-factor expression and the conditional angular sampling against numerical integration.

The optical effective area is calculated as

$$A_{\mathrm{eff,opt}}(E) = A_{\mathrm{inc}} \frac{N_{\mathrm{fp}}(E)}{N_{\mathrm{inc}}(E)}, \tag{3}$$

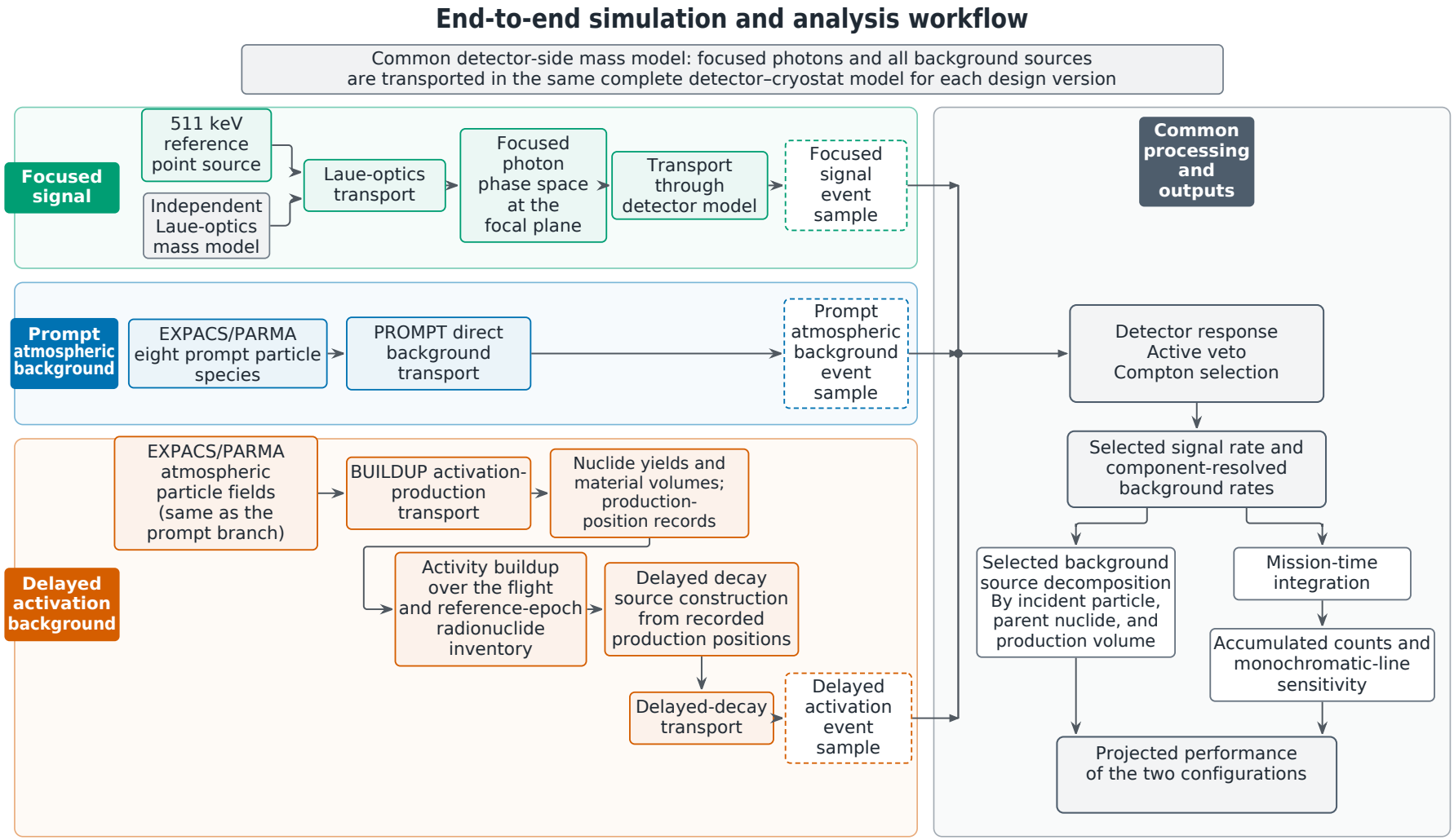

Fig. 3 End-to-end simulation and analysis workflow. The focused signal, prompt atmospheric background, and delayed activation form three physical branches. The prompt branch comprises eight independently normalized particle species ($\gamma, e^-, e^+, \mu^-, \mu^+, n, p, \alpha$). All streams undergo the common detector response, active veto, and Compton event selection within each mass model.

where $N_{\rm inc}$ is the number of photons sampled over the projected crystal area and $N_{\rm fp}$ counts diffracted photons intercepting a circular aperture of radius 18.98 mm at the 10 m focal plane. Three independent samples, each with 50,000 incident photons, yielded a combined $N_{\rm fp} = 37{,}175$ from $N_{\rm inc} = 150{,}000$, giving $A_{\rm eff,opt}(511\,{\rm keV}) = (19.717 \pm 0.089)\,{\rm cm}^2$, where the uncertainty is one Monte Carlo standard error. This area includes crystal transport and geometrical interception; window transmission, detector response, and event selection are accounted for in the detector-coupled calculation. The sensitivity estimates use this single-ring reference lens model as a common optical baseline for comparing the focal-plane cryostat configurations.

Here the reference signal is a monochromatic 511 keV point source. Its reference normalization is $F_{\rm ref} = 2.4 \times 10^{-4}\,{\rm ph\,cm^{-2}\,s^{-1}}$ above the atmosphere (Section 3.4), motivated by the dedicated INTEGRAL/IBIS point-source upper limit [10]. It is constructed as a MEGAlib far-field source [24], with the detailed construction given in Section 3.2.3. The primary background budget is defined for the detector/cryostat branch, while the optics branch supplies the transported focal-plane signal phase space.

3.2 Source construction

The reference point-source EventList, the prompt atmospheric field, and the delayed-decay source are constructed independently. The eight prompt particle species retain separate physical-rate normalizations; activation production and delayed decay remain separate transport stages.

3.2.1 Prompt atmospheric source

The prompt atmospheric field is derived from EXPACS/PARMA. PARMA is an analytical model parameterized from PHITS atmospheric-shower calculations and benchmarked against terrestrial cosmic-ray measurements, and EXPACS is its public tabulation and software interface [31, 32]. PHITS supplies the underlying particle-transport physics: primary cosmic rays interact with air nuclei, the secondary hadrons, leptons, photons, and neutrons are transported through the atmospheric column, and the resulting fluences are parameterized by altitude, geomagnetic cutoff, solar modulation, energy, and direction. In this work EXPACS/PARMA provides the differential incident flux as a function of particle species, kinetic energy, zenith angle, geographic position, altitude, cutoff rigidity, and solar activity. The transport templates use a reference environment at latitude 34° N, longitude 100° E, and altitude $38\,{\rm km}$, with vertical cutoff rigidity $R_c = 11.6\,{\rm GV}$ and the 2025-08-31 solar condition corresponding to $W = 118.3$.

The prompt source includes photons, neutrons, electrons, positrons, protons, alpha particles, and negative and positive muons. For each particle species the EXPACS/PARMA differential spectrum is converted into a MEGAlib far-field area source covering the full zenith range $\theta = 0^\circ$–180° and full azimuth range $\phi = 0^\circ$–360°. The zenith dependence is represented by 20 equal-μ bins, where $\mu = \cos\theta$: the first ten are down-going and the last ten up-going or albedo-like. Figure 4 shows the resulting energy spectra and angular distributions. We omit the extragalactic diffuse continuum [33] from the balloon prompt-background model because its directly transmitted flux is about 2% of the PARMA atmospheric photon flux over 0.515–$29.5\,{\rm MeV}$.

The full-sphere integrated fluxes in the adopted atmospheric tables are 4.800, 0.4622, 0.1990, 0.1170, 0.1123, 0.01149, 0.004969, and $0.005570\,{\rm cm^{-2}\,s^{-1}}$ for γ, n, e^-, e^+, p, α, μ^-, and μ^+, respectively.

If $I_j(E,\mu)$ denotes the EXPACS/PARMA differential intensity for species j, the flux carried by equal-μ bin m is

$$\Phi_{j,m} = 2\pi \int_{\mu_m^-}^{\mu_m^+} {\rm d}\mu \int I_j(E,\mu)\,{\rm d}E, \qquad \Delta\mu = 0.1, \tag{4}$$

where μ_m^- and μ_m^+ are the lower and upper cosine bounds of bin m. Each bin subtends $\Delta\Omega = 2\pi\Delta\mu = 0.6283\,{\rm sr}$.

All eight particle species use a far-field area source of radius $R = 60\,{\rm cm}$. For each sampled direction, starting positions are drawn uniformly from the projected disk perpendicular to that direction, and momenta point into the mass model; the geometric rate factor is the projected area πR^2. Together, the 20 bins cover 4π incident solid angle. The same atmospheric-field definition is used separately for prompt transport and activation-production calculations.

Each accepted independent simulation run for particle species j contains the complete 20-bin angular mixture. The species source rate and the merged equivalent exposure are

$$\dot{N}_j^{\rm src} = \pi R^2 \sum_{m=1}^{20} \Phi_{j,m}, \qquad T_{g,j}^{\rm eq} = \sum_{q\in\mathcal{Q}_{g,j}} {\rm TT}_{g,j,q} \simeq \frac{\sum_q N_{g,j,q}^{\rm sim}}{\dot{N}_j^{\rm src}}, \qquad w_{g,j}^{\rm pr} = \frac{1}{T_{g,j}^{\rm eq}}, \tag{5}$$

where g labels the mass model, $\mathcal{Q}_{g,j}$ is the set of accepted independent transport samples, q indexes these samples, and ${\rm TT}_{g,j,q}$ is the physical exposure represented by each sample.

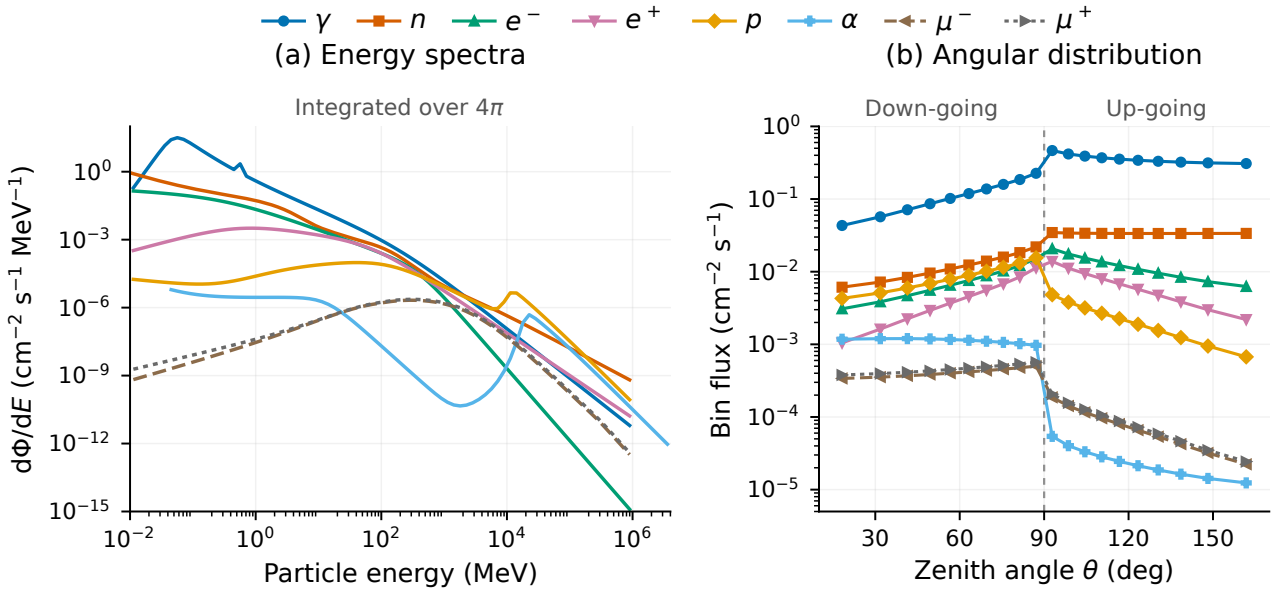

Fig. 4 EXPACS/PARMA atmospheric particle field used for prompt transport and activation production. (a) Differential energy spectra integrated over solid angle, shown above 10 keV. E denotes photon energy or total kinetic energy per incident particle. (b) Fluxes in the 20 equal-μ zenith bins ($\mu = \cos\theta$), integrated over the full sampled energy range. Colors identify the same particle species in both panels. The reference environment is latitude 34°, longitude 100°, altitude 38 km, $R_c = 11.6$ GV, and $W = 118.3$

3.2.2 Delayed activation source

The delayed source is built from a separate activation-production transport. This stage records the nuclide, material volume, incident species, and stopping position of each radioactive product retained for delayed transport. Ground-state half-lives are checked against NUBASE2020 [34], and the decay of ^{158}Er is simulated using Geant4 RadioactiveDecay 6.1.2 with the corresponding ^{158}Ho level data from PhotonEvaporation 6.1. Nuclide activities include direct production and feeding from radioactive parents. For nuclear state k, $A_k(t) = \lambda_k N_k(t)$, with $\lambda_k = \ln 2/t_{1/2,k}$. The reference epoch is $t_{\mathrm{flight}} = 15$ d; the inventory evolution is defined in Section 3.4. The balloon is expected to operate for 10–20 d, and day 15 is adopted as a representative activation reference within this interval. The 20 d on-source projection and the 0, 5, 10, 15, and 20 d sampled mission times are defined separately in Section 3.4.

The simulated activation products retain the nuclide identities and stopping positions used to construct the delayed source. Direct production is normalized separately for each incident-particle species using its activation-production exposure. Daughter feeding is included in the inventory evolution, while the original production material and position are retained for source tracing.

Retaining the production positions is essential because the ability of a delayed particle to escape the surrounding material, trigger the geometry-specific active anticoincidence, or pass the Compton event selection depends on where it was produced. Charged particles also lose energy with increasing penetration depth, changing the relative contributions of activation mechanisms and the reaction cross sections for different products. For the photon-induced Under-stage sample and the Lateral-chimney samples, the decay transport used 10^4 activation-position point sources for each incident-particle species with nonzero delayed-source activity. Source nuclides were sampled by their day-15 activities in each production volume, with positions drawn uniformly from the matched production coordinates. Additional decays were simulated for selected nuclear states with known sampling probabilities. The normalization includes all simulated decay events, including those with no detector energy deposit. Each daughter response retains the original activation product's identity and position, separately from the identity of the decaying nuclide.

For the seven non-γ species in Under-stage, the decay response uses a pooled inventory of 222,052 production points, normalized separately by the activation-production exposure of each species. For each of p, α, n, e^+, e^-, and μ^-, 10^6 decay histories were simulated from explicitly sampled nuclear states: 850,000 in non-BGO materials and 150,000 in BGO. Within each material stratum, production points and decaying states were sampled using their peak physical source rates over the 81 mission nodes. Event weights account for the sampling probabilities and the total number of histories in that species and material stratum. The μ^+ response uses 10^6 ^{71}Ge decay histories from four samples of 250,000 histories, each weighted by its activity normalization. In the sampled μ^+ activation inventory, the remaining ^{208}Bi contributes fewer than 3.1×10^{-4} expected de-

cays over 20 d.

Decay responses are normalized separately for each configuration and incident-particle species. Each event is weighted by the time-dependent activity of its decaying nuclear state divided by the corresponding sampling normalization. For the point-source decay samples, this normalization accounts for the finite transport exposure and daughter decays generated during it. For independently sampled states, it uses the number of simulated decays and their sampling probabilities, including decays with no detector energy deposit.

3.2.3 Reference point-source construction

The focused-signal branch uses an on-axis monochromatic $511\,\mathrm{keV}$ far-field point source, represented by a parallel beam at the lens entrance. The flux convention and atmospheric attenuation of the reference source are defined in Section 3.4; this subsection specifies only the focal-plane photon phase space and the signal-retention calculation.

Photons are sampled uniformly over the lens aperture A_{inc} defined by Equation (3). The 30 arcsec mosaic spread, XOP/CRYSTAL rocking curve, and 10 m geometry set the focal-plane response. At 10 m, $r_{90} = 0.99\,\mathrm{cm}$ and $r_{99} = 1.17\,\mathrm{cm}$ correspond to 3.40 and 4.02 arcmin. The accepted photon phase space forms the common EventList for both mass models.

For mass model g, let $N_{\mathrm{sel},g}$ be the number of focal-plane photons retained after detector transport, response convolution, analysis-window selection, active anticoincidence, and the Compton event selection. The total isolated-event signal-retention fraction is

$$\epsilon_{\mathrm{sig},g} = \frac{N_{\mathrm{sel},g}}{N_{\mathrm{fp}}}. \tag{6}$$

The retention of an individual selection stage k is defined relative to the signal entering that stage,

$$\epsilon_{k,g} = \frac{N_{k,g}}{N_{k-1,g}}, \tag{7}$$

where $N_{k-1,g}$ and $N_{k,g}$ are the signal counts immediately before and after the selection. The same Compton reconstruction is used for both models, with compatibility evaluated against the focal spot.

3.3 Detector response, event selection, and veto definitions

The simulation samples the focused signal, prompt atmospheric backgrounds, and delayed activation as independent Poisson streams at their physical rates and merges them onto one time axis before detector response, analysis-window selection, active anticoincidence, and Compton selection. The eight prompt particle species retain independent physical-rate normalizations.

3.3.1 Time axis and rate normalization

In a stationary radiation environment, mutually independent particle events with a constant mean arrival rate have Poisson-distributed counts in a fixed time interval. Conditional on the event count, their arrival times are uniformly distributed within that interval. This provides a natural temporal representation for rate-normalized Monte Carlo event samples: each sample supplies the energy deposits, positions, and topologies, while the Poisson process determines how often and when those events occur on the physical time axis.

Motivated by the nanosecond timing capability reported for BGO detectors and microsecond arrival-time estimates derived from TES pulse rising edges, we adopt a reference coincidence time scale of $1\,\mu\mathrm{s}$.

The radiation environment evolves along the balloon trajectory, but much more slowly than the $1\,\mu\mathrm{s}$ coincidence time scale adopted in this study. Within each trajectory node, the event streams can therefore be approximated as independent Poisson processes with constant arrival rates. The prompt atmospheric and delayed-activation backgrounds are generated by separate transport calculations and do not share a physical time axis, whereas the geometry-specific active anticoincidence and Compton event selections depend on all energy deposits within the same time window. Evaluating accidental coincidences therefore requires these event samples to be mapped onto a common time axis.

Each event sample carries per-event rate weights r_{km} from its source normalization. Here k labels the focused signal or a separately normalized prompt or delayed event sample for one particle species, and m labels a simulated event. The total rate of sample k is $R_k = \sum_m r_{km}$. For a reference interval of duration T, the number of instances drawn from sample k is

$$N_k \sim \mathrm{Pois}(R_k T). \tag{8}$$

Simulated events are sampled with replacement with probabilities r_{km}/R_k and are assigned independent uniform times in $[0, T]$. The resulting sequence preserves both the physical rate and the energy, direction, and detector-response distribution of the event stream.

Decays in the same chain separated by no more than $\tau = 1\,\mu$s are combined into one response before Poisson time-stream superposition. The independent signal and background draws are then merged and ordered by arrival time. Events separated by no more than τ are linked transitively into one coincidence cluster c. Here τ is the adopted anticoincidence window. All energy deposits in the cluster are subjected jointly to the analysis-window, geometry-specific active-anticoincidence, and Compton event selections. Figure 5 summarizes this construction.

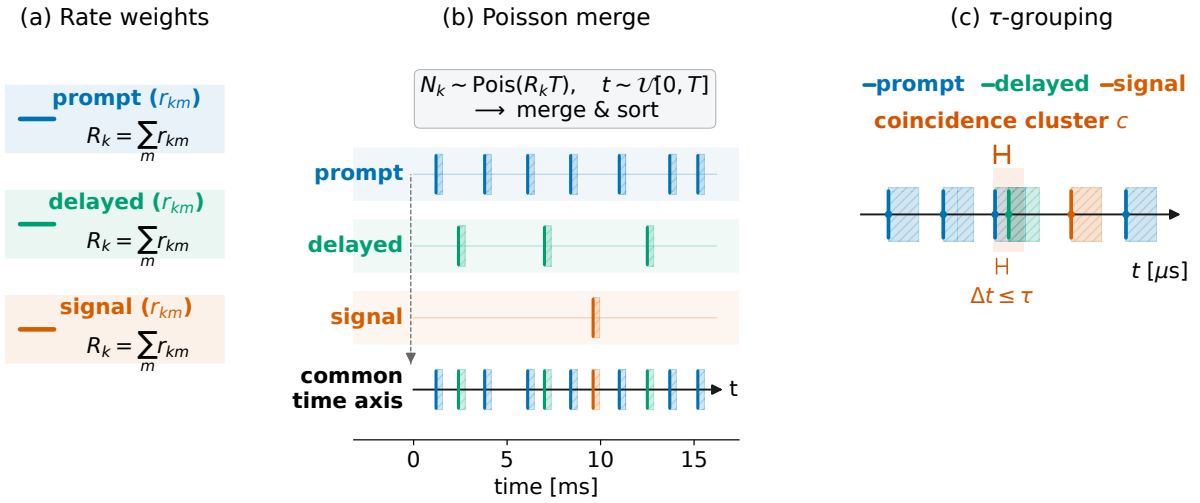

Fig. 5 Schematic construction of the common time axis for coincidence grouping. (a) Each transported stream carries per-event rate weights and a total rate. (b) Independent Poisson draws are merged and time-ordered on a common axis; T is the sampled physical interval at one trajectory node. (c) Consecutive events separated by no more than $\tau = 1\,\mu$s are linked into one coincidence cluster c. Colors identify stream membership; event positions and densities are schematic

The simulation is repeated at days 0, 5, 10, 15, and 20 using the physical rates at each epoch. These equally spaced sampling times span the projection interval and check its time evolution.

Instrument performance is then evaluated along the long-duration balloon trajectory, with the 20 d on-source projection sampled at 6 h intervals. Particle fluxes, atmospheric transmission of the signal, and the activation inventory evolve with flight time and position, thereby changing both the event density on the common time axis and the accidental-coincidence probability. The background corrections and signal-retention fractions obtained at the five reference times are applied along the full trajectory. Section 3.4 specifies the trajectory model, temporal interpolation, and cumulative-count calculation.

3.3.2 Detector response, analysis energy window, and weighted rates

Before the analysis-window and anticoincidence decisions, TES energy deposits in each coincidence cluster are combined by pixel identifier. Multiple deposits in the same pixel are summed to give its deposited energy. The pixel identifier links the measured energy to the pixel geometry used in Compton reconstruction. The adopted single-pixel energy resolution is $\Delta E_{\mathrm{FWHM}} = 500\,\mathrm{eV}$; TES measurement fluctuations are approximated by a Gaussian response with this FWHM. Pixel hits with measured energies below $0.300\,\mathrm{keV}$ are removed.

The measured energies of all retained TES pixel hits are summed to give the total measured TES energy of the event, which is used for the 511 keV analysis-window selection. The measured energy, pixel identifier, layer, and hit multiplicity remain available for the subsequent Compton event selection. BGO deposits are accumulated separately, are not included in the TES total, and enter the active anticoincidence decision in the next subsection.

The common analysis energy window of interest has a fixed one-FWHM half-width: $510.50 \le E_{\mathrm{TES}} < 511.50\,\mathrm{keV}$ for the focused signal and all backgrounds.

For each configuration and initiating-particle species, the delayed-decay sample size is $N = 1{,}000{,}000$.

The simulated event samples have different physical fluxes, transport exposures, and source-level reweighting. Each event therefore carries a physical-rate weight. For isolated-event selection, the signal or background rate at a given stage is obtained by summing the weights of events that pass that stage. Monte Carlo statistical uncertainties are propagated from the actual weight distribution, while focused-signal acceptance is treated binomially using the common focal-plane sample. Long-duration rate propagation along the mission trajectory is described in Section 3.4; the response-convolved spectra through the active-veto and Compton-selection stages are reported with the cut-flow results.

3.3.3 Active anticoincidence selection

Active anticoincidence rejects events that produce a 511 keV candidate in the TES while also depositing energy in the surrounding active shield. Passive shielding attenuates incident radiation, whereas active BGO provides time-coincident information for event-by-event discrimination. A focused 511 keV photon reaches the TES mainly through the optical entrance aperture. Atmospheric charged particles, secondaries from hadronic interactions, and some high-energy atmospheric-γ cascades are more likely to deposit energy in both the TES and the surrounding active volumes. Coincident BGO energy can therefore identify background candidates in the analysis energy window.

Following the TES response and analysis-window selection in Section 3.3.2, simulated energy deposits in all BGO volumes within each coincidence cluster are summed as E_{BGO}.

The active system of the Under-stage reference comprises a BGO side shell, bottom cap, and top cap. The cluster-level passing condition is

$$E_{\mathrm{BGO}} < 50\,\mathrm{keV}.$$

The common offline threshold is applied to the cluster-summed BGO deposit; $E_{\mathrm{BGO}} \geq 50\,\mathrm{keV}$ vetoes the cluster.

The cluster-summed deposits include both correlated TES–shield deposits from one incident particle and accidental overlap of otherwise independent hits whose arrival times satisfy the $1\,\mu$s linking rule. A focused photon can therefore be rejected when an unrelated active-shield hit enters the same coincidence cluster. The associated loss is described by the accidental signal-survival fraction defined in Section 3.4 and included in the mission-time integration. Candidates that pass the active selection proceed to the Compton event selection.

3.3.4 Compton event selection

Active anticoincidence removes candidates with energy deposits above the adopted threshold in the surrounding scintillators, but it cannot distinguish a focused photon from a background event whose interactions remain within the TES array. Either can leave a total energy near 511 keV in the focal plane. A focused photon must, however, arrive through the optical entrance aperture. For an event with two or more separated TES hits, the division of energy among the hits and their relative positions constrain the possible arrival directions. We therefore use the kinematic cone construction of a Compton camera [24] to test whether each event is compatible with the focal spot.

The six-layer pixelated TES focal plane provides the information needed for this test at pixel scale. For the retained hits defined in Section 3.3.2, the response model supplies a measured energy and a pixel identifier. The identifier specifies the TES layer and the pixel's geometric center and vertices. Hits in different pixels or layers therefore provide both an energy division and a finite spatial lever arm. The reconstruction treats the interaction order and the position within each pixel as unknown. A single-hit event consequently carries no Compton-direction information and is retained as a calorimetric line candidate; multi-hit events proceed to the consistency test below.

For an assumed interaction order, let a candidate of total energy E_0 deposit E_1 at the first representative position $\mathbf{r}_1$ and then propagate with $E_{\mathrm{sc}} = E_0 - E_1$ to a second position $\mathbf{r}_2$. The measured energies give the Compton scattering angle

$$\cos\theta_C = 1 - m_e c^2 \left(\frac{1}{E_{\mathrm{sc}}} - \frac{1}{E_1 + E_{\mathrm{sc}}} \right). \tag{9}$$

The vector $\mathbf{r}_2 - \mathbf{r}_1$ fixes the scattered-photon direction $\hat{\mathbf{u}}_{12}$, but not the incident direction. Together, $\hat{\mathbf{u}}_{12}$ and θ_C define a cone of allowed source directions with apex $\mathbf{r}_1$ and axis $-\hat{\mathbf{u}}_{12}$. The event is retained if the cone intersects the focal spot in the focal-plane entrance plane.

For each hit, nine representative positions are taken from the physical pixel: its eight vertices and geometric center. For an assumed order of the first two hits, their representative points give $9 \times 9 = 81$ position pairs and hence 81 candidate cones. One intersection among the 81 candidate cones is sufficient to retain that order. Figure 6 summarizes this construction.

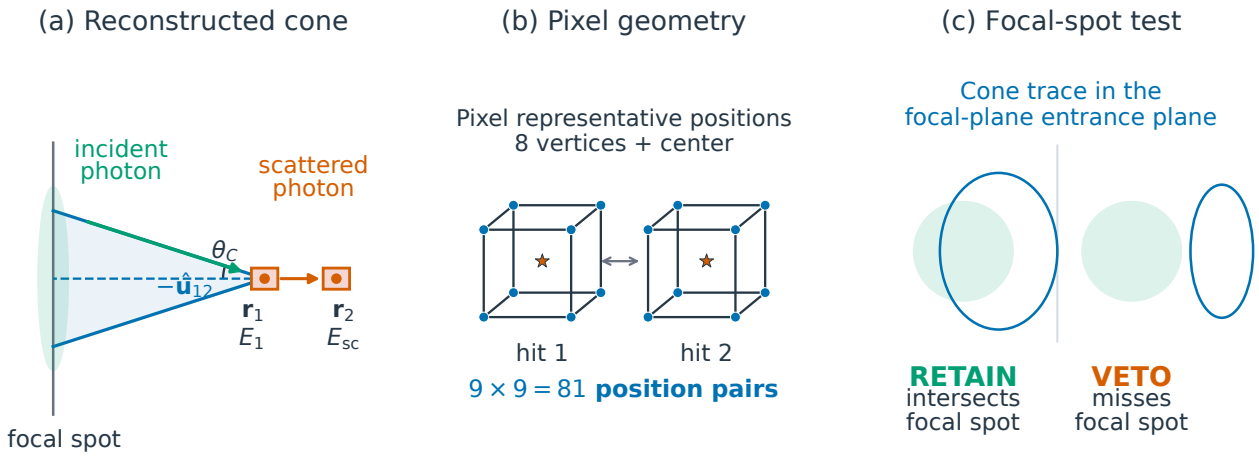

Fig. 6 Schematic of the Compton event selection. (a) The first two TES hits define a reconstruction cone from their measured energies and representative positions; the cone is a set of allowed source directions. (b) Each hit is represented by the eight vertices and geometric center of its physical pixel, transformed into the common reconstruction frame. The first two pixels give $9 \times 9 = 81$ position hypotheses for a specified order. (c) The curves show cone traces in the focal-plane entrance plane. An intersection with the focal spot retains the event, whereas a valid reconstruction that misses the spot is vetoed. Events without a valid cone remain in the rate accounting as unreconstructed. The schematic is not to scale

The interaction order is treated separately from the within-pixel position uncertainty. For a two-hit event, both orders are tested and either compatible order is sufficient. For an event with three to six hits, all orders are first enumerated using the geometric centers of the hit pixels. For a candidate sequence of n hits $\{(\mathbf{r}_j, \epsilon_j)\}_{j=1}^{n}$, where $\mathbf{r}_j$ is the pixel center used for sequence ranking, the Compton sequence residual is

$$Q = \sum_{i=2}^{n-1} \left(\cos\theta_{C,i} - \hat{\mathbf{u}}_{i-1,i} \cdot \hat{\mathbf{u}}_{i,i+1}\right)^2 , \tag{10}$$

where $\theta_{C,i}$ is calculated from the energy ϵ_i deposited at hit i and the remaining energy $\sum_{k=i+1}^{n} \epsilon_k$; the two unit vectors describe the adjacent flight segments. Orders without a physical Compton solution do not enter the ranking. We select the order with the smallest Q; if two orders are tied, we choose the one with the longer first lever arm. Only the first-scatter cone of this selected order receives the 81-position focal-spot test.

A reconstructable multi-hit event is vetoed only when the cone or cones tested under the applicable ordering rule miss the focal spot. If no candidate order has a physically valid solution, the event is marked as unreconstructed and retained in the final rate. Events with more than six retained pixel hits are also kept as unreconstructed.

3.4 From the day-15 reference result to mission-time evolution

For the mission-time integration, we rescale the 2σ INTEGRAL/IBIS point-source upper limit of $1.6 \times 10^{-4}\,\mathrm{ph\,cm^{-2}\,s^{-1}}$ for a 10 Ms exposure toward the Galactic center [10] linearly from 2σ to 3σ under the Gaussian approximation and set the top-of-atmosphere reference flux to $F_{\mathrm{ref}} = 2.4 \times 10^{-4}\,\mathrm{ph\,cm^{-2}\,s^{-1}}$. At each trajectory node, the mission-time integration calculates atmospheric transmission from the residual column depth at the assumed balloon altitude and a fixed 27° reference elevation. The representative reference state is the day-15 trajectory node at 38.75 km; the adopted residual column at this node gives $T_{\mathrm{ref}} = 0.514$. The corresponding telescope-incident reference flux is $F'_{\mathrm{ref}} = F_{\mathrm{ref}} T_{\mathrm{ref}} = 1.233 \times 10^{-4}\,\mathrm{ph\,cm^{-2}\,s^{-1}}$. At other trajectory nodes, the incident flux is $F_{\mathrm{ref}} T_{\mathrm{atm},511}(t)$, and minimum detectable fluxes are reported before atmospheric attenuation.

Detector transport supplies component-response templates at 38 km. The mission-time calculation holds these responses fixed while propagating the focused signal, eight prompt species, and delayed activation over the evolving environment and inventory [16, 35].

To cover the expected 10–20 d balloon operation, the synthetic reference trajectory spans 0–20 d in 81 nodes separated by 0.25 d. Its altitude ranges from 36.25 to 41.25 km, its latitude from 33.75° to 34.25° N, and its longitude from 99.75° to 100.25° E. At day 15, the reference state is 38.75 km, 34° N, and 100° E. At 34° N, the Galactic center culminates at 27°, giving the minimum line-of-sight atmospheric column toward the source. Altitude changes affect both the incident particle field and the atmospheric transmission at 511 keV; latitude and longitude provide a controlled geomagnetic modulation. The trajectory provides the same 20 d on-source exposure for both mass models. Because the comparison is defined for equal on-source exposure rather than a specific observing schedule, target visibility, occultation of the target by the Earth, and repointing intervals are not included in this integration.

For a specified top-of-atmosphere 511 keV line flux, the focused-signal rate before accidental-coincidence correction is scaled by the atmospheric transmission,

$$S_g^{\rm dir}(t) = S_g^{\rm dir}(t_{15})\frac{T_{\rm atm,511}(t)}{T_{\rm atm,511}(t_{15})} = F_{\rm TOA,511}A_{\rm eff,opt}(511\,{\rm keV})\epsilon_{{\rm sig},g}T_{\rm atm,511}(t), \tag{11}$$

where g denotes the mass model and $\epsilon_{{\rm sig},g}$ is the total signal-retention fraction defined in Equation (6). In the plane-parallel attenuation model [22], $T_{\rm atm,511}(t) = \exp[-\mu_{\rm eff}X(t)/\sin\epsilon]$. We adopt $\mu_{\rm eff} = 0.08736\,{\rm cm^2\,g^{-1}}$, normalized to a reference vertical transmission of 0.7390 at a residual column of $3.461\,{\rm g\,cm^{-2}}$. At day 15, with $\epsilon = 27^\circ$, this gives $T_{\rm atm,511}(t_{15}) = 0.514$. The time integration recalculates this transmission at every trajectory node.

Prompt background is scaled separately for each incident species a,

$$R_{{\rm prompt},g,a}(t) = R_{{\rm prompt},g,a}(t_{15})\frac{\Phi_a(t)}{\Phi_a(t_{15})} = \Phi_a(t)K_{g,a}, \tag{12}$$

where $\Phi_a(t)$ is the node flux and $K_{g,a}$ is the selected response coefficient of the transport template. The energy and angular templates for each species remain fixed across the trajectory nodes.

The activation inventory is evolved separately for each incident-particle species and production location. The direct production rate of nuclear state k from species a is

$$P_{g,a,k}(t) = P_{g,a,k}(t_{15})\frac{\Phi_a(t)}{\Phi_a(t_{15})} = \Phi_a(t)Y_{g,a,k}, \tag{13}$$

where $Y_{g,a,k}$ is fixed by the simulated production sample. The production rates are interpolated linearly between adjacent time nodes. The inventory satisfies

$$\frac{{\rm d}N_{g,a,k}}{{\rm d}t} = P_{g,a,k}(t) - \lambda_k N_{g,a,k}(t) + \sum_j b_{j\to k}\lambda_j N_{g,a,j}(t), \qquad A_{g,a,k}(t) = \lambda_k N_{g,a,k}(t), \tag{14}$$

where $b_{j\to k}$ is the decay branching fraction from state j to k. Stable daughters terminate the chains; short-lived intermediate levels are included through their decay branches. The initial condition is $N_{g,a,k}(0) = 0$, excluding activation before the first trajectory node. The selected delayed rate is

$$R_{{\rm delayed},g}(t) = \sum_a\sum_k A_{g,a,k}(t)\varepsilon_{g,a,k}, \tag{15}$$

where the response coefficients retain the corresponding production-location distribution. Each coefficient includes the probability that the decay starts a separate coincidence cluster; a daughter decay occurring within τ of the preceding decay is included in that cluster's response.

The total background rate before accidental-coincidence correction is

$$B_g^{\rm dir}(t) = \sum_a R_{{\rm prompt},g,a}(t) + R_{{\rm delayed},g}(t). \tag{16}$$

At the five sampled mission times defined in Section 3.3.1, the superposed streams undergo the same response and event selections; the resulting background correction is

$$C_{{\rm bg},g,r} = \frac{n_{g,r}^{\rm tl}/T_{g,r}^{\rm sim}}{B_g^{\rm dir}(t_r)}. \tag{17}$$

$C_{{\rm bg},g,r}$ converts the isolated-event background to the rate after Poisson time-stream superposition, accounting for net accidental-coincidence effects including random vetoing and energy pile-up into the analysis window. Here r labels the sampled mission time, $T_{g,r}^{\rm sim}$ is its simulated exposure, and $n_{g,r}^{\rm tl}$ is its selected background count. At each sampled time, $\widehat{\eta}_{g,r}$ is the fraction of isolated-event selected signal events that remain selected after the signal, prompt, and delayed streams are superposed. The background correction and focused-signal retention are interpolated separately between adjacent sampled times.

The final time-dependent rates are

$$S_g(t) = S_g^{\rm dir}(t)\eta_g(t), \qquad B_g(t) = B_g^{\rm dir}(t)C_{{\rm bg},g}(t). \tag{18}$$

Trapezoidal integration over the 81 nodes then gives the cumulative counts at exposure T_n,

$$\begin{aligned} N_s(T_n) &= \sum_{\ell=1}^{n}\frac{S_g^{\rm dir}(t_{\ell-1})\eta_g(t_{\ell-1}) + S_g^{\rm dir}(t_\ell)\eta_g(t_\ell)}{2}\,\Delta t_\ell, \\ N_b(T_n) &= \sum_{\ell=1}^{n}\frac{B_g^{\rm dir}(t_{\ell-1})C_{{\rm bg},g}(t_{\ell-1}) + B_g^{\rm dir}(t_\ell)C_{{\rm bg},g}(t_\ell)}{2}\,\Delta t_\ell. \end{aligned} \tag{19}$$

The resulting $N_s(T)$ and $N_b(T)$ are the inputs to the sensitivity definition in the next subsection. The cumulative counts are reported in Section 4.5.

3.5 Mission significance and minimum detectable line flux

For cumulative signal and background counts, we define the counting significance as

$$Z(T) = \frac{N_s(T)}{\sqrt{N_b(T)}}. \tag{20}$$

Under the high-count, weak-signal conditions considered here, this is the large-sample limit of the Poisson counting likelihood for $N_s \ll N_b$ [36].

At fixed exposure, the focused-signal count is proportional to the target line flux. In the weak-source approximation, changing this flux leaves the atmospheric-particle and activation background counts unchanged. The $q\sigma$ minimum detectable top-of-atmosphere line flux at exposure T is therefore

$$F_{q\sigma}(T) = F_{\mathrm{ref}} \frac{q}{Z(T; F_{\mathrm{ref}})}, \qquad q \in \{3, 5\}. \tag{21}$$

The time required to reach a specified significance is the first crossing of $Z(T) = q$.

The same transport events are reused at all 81 mission nodes, so their statistical errors are correlated across time. We first accumulate each event's weighted contribution over all nodes and then calculate the statistical uncertainty of the mission-integrated counts. Statistical errors from the decay and prompt response samples, five sampled mission times, optical sampling, and signal retention are propagated to the 20 d flux thresholds. Threshold-crossing times are linearly interpolated between adjacent nodes. The quoted Monte Carlo errors are conditional on the simulated activation-production inventory; uncertainty in that inventory and model systematic errors are not included.

4 Results

We first trace Under-stage backgrounds to their physical origins, then compare Lateral-chimney on the common mission time axis. For presentation, the prompt branch is separated into atmospheric γ rays and the seven non-γ species.

4.1 Baseline background and selection performance of Under-stage

Under-stage defines the reference performance. Table 1 gives the day-15 cut flow for isolated events in the $[510.50, 511.50)\,\mathrm{keV}$ analysis energy window. The active-BGO selection reduces the total background rate from $5.709\,\mathrm{s}^{-1}$ (15,848 simulated events) to $5.618 \times 10^{-2}\,\mathrm{s}^{-1}$ (1,196 events), removing 99.02% of the pre-veto rate. Across the seven non-γ prompt particle species ($T^{\mathrm{eq}} \approx$ 1599–1613 s), only one positron event at $6.038 \times 10^{-4}\,\mathrm{s}^{-1}$ survives the active veto and final selection, whereas the atmospheric-γ component falls from $2.592\,\mathrm{s}^{-1}$ to $1.829 \times 10^{-2}\,\mathrm{s}^{-1}$, and delayed activation falls from $0.2489\,\mathrm{s}^{-1}$ to $3.729 \times 10^{-2}\,\mathrm{s}^{-1}$.

After the Compton event selection, 1,083 simulated background events remain at $4.958 \times 10^{-2}\,\mathrm{s}^{-1}$, or 88.25% of the active-veto rate. All 28,394 isolated focused-signal events in the measured window pass the active selection, and 27,426 survive the final selection. The Compton selection therefore retains 96.59% of the signal passing active anticoincidence. Active anticoincidence supplies most of the rate reduction, while the Compton selection removes a smaller residual and retains most of the focused signal.

Table 1: Under-stage analysis-window cut flow at 500 eV FWHM. Background entries are day-15 isolated-event counts and rates; signal entries give counts and retention relative to the signal in the analysis energy window before active anticoincidence.

Stream	Pre-veto	After active veto	Final selection
Non-γ prompt	4711 / $2.868\,\mathrm{s}^{-1}$	1 / $6.038 \times 10^{-4}\,\mathrm{s}^{-1}$	1 / $6.038 \times 10^{-4}\,\mathrm{s}^{-1}$
Atmospheric γ	5613 / $2.592\,\mathrm{s}^{-1}$	40 / $1.829 \times 10^{-2}\,\mathrm{s}^{-1}$	34 / $1.552 \times 10^{-2}\,\mathrm{s}^{-1}$
Delayed activation	5524 / $0.2489\,\mathrm{s}^{-1}$	1155 / $3.729 \times 10^{-2}\,\mathrm{s}^{-1}$	1048 / $3.346 \times 10^{-2}\,\mathrm{s}^{-1}$
Total background	15848 / $5.709\,\mathrm{s}^{-1}$	1196 / $5.618 \times 10^{-2}\,\mathrm{s}^{-1}$	1083 / $4.958 \times 10^{-2}\,\mathrm{s}^{-1}$
Focused signal	28394 / 100%	28394 / 100%	27426 / 96.59%

The nonzero components of the final isolated-event background are delayed activation, atmospheric γ rays, and non-γ prompt particles (Table 2). Delayed activation contributes $3.346 \times 10^{-2}\,\mathrm{s}^{-1}$ (67.49%), the atmospheric-γ component contributes $1.552 \times 10^{-2}\,\mathrm{s}^{-1}$ (31.29%), and the non-γ prompt component contributes $6.038 \times 10^{-4}\,\mathrm{s}^{-1}$ (1.22%).

Table 2: Day-15 final isolated-event background of Under-stage at 500 eV FWHM. Standard errors and effective sample sizes use $\sum_i w_i^2$.

Component	Events	Rate / cps	Error / cps	N_{eff}	Share / %
Non-γ prompt	1	6.038×10^{-4}	6.038×10^{-4}	1.00	1.22
Atmospheric γ	34	1.552×10^{-2}	2.667×10^{-3}	33.84	31.29
Delayed activation	1048	3.346×10^{-2}	1.544×10^{-3}	469.68	67.49
Total	1083	4.958×10^{-2}	3.141×10^{-3}	249.23	100.00

4.2 Background origins and spatial coupling in Under-stage

The preceding subsection establishes the background level of Under-stage. To identify its physical origins, we traced all final events by initiating particle species. The delayed-activation component was further decomposed by parent-production material, source-volume/parent-nuclide pair, and spatial region relative to the TES. Here the parent nuclide denotes the initially produced activation product; its contribution includes selected decays of its radioactive descendants.

Proton-induced activation is the largest single contribution, at $1.760 \times 10^{-2}\,\mathrm{s}^{-1}$ (184 simulated events), or 35.50% of the total isolated-event background. The remaining delayed terms are $9.077 \times 10^{-3}\,\mathrm{s}^{-1}$ from neutron-induced activation, $6.363 \times 10^{-3}\,\mathrm{s}^{-1}$ from α-induced activation, $3.261 \times 10^{-4}\,\mathrm{s}^{-1}$ from e^+-induced activation, $7.850 \times 10^{-5}\,\mathrm{s}^{-1}$ from γ-induced activation, $1.210 \times 10^{-5}\,\mathrm{s}^{-1}$ from e^--induced activation, and $1.839 \times 10^{-6}\,\mathrm{s}^{-1}$ from μ^--induced activation.

In the material decomposition, copper accounts for 59.47% of the final delayed rate. The leading source-volume/nuclide contributions are ^{62}Cu produced in the TES support cold plates and the TES copper heat-sink ring.

Grouping the parent-production sites by transport component identifies the TES substrate-support copper panels as the largest copper source, at 27.83% of the final delayed rate. The MC cold plate and TES-stack copper heat-sink ring contribute 14.91% and 10.92%, respectively. The Bi passive-shield layer, the remaining dilution-refrigerator/cold-stage hardware, the remaining detector-bay components, and aluminum cryostat and shield components contribute 25.34%, 8.46%, 6.84%, and 5.70%, respectively. An independent spatial projection assigns 20.03% of the delayed rate to the DR mixing chamber and staged cold region.

Figure 7 projects the same final selected delayed-activation events onto their parent-production components and initiating primary-particle species. The component projection resolves the cold plate, TES supports, and heat sink, while the projection by particle species identifies protons, neutrons, and α particles as the main drivers of this component.

Surrounding a main detector with active anticoincidence counters is an established low-background strategy in hard-X-ray and soft-γ-ray instruments; the Suzaku/HXD, for example, used thick BGO guard counters around its main detector units [37]. BGO is placed outside the cryostat to cover the refrigerator body without cooling the scintillator to cryogenic temperatures, where its longer scintillation decay would impede fast anticoincidence [38]. Keeping its optical readout outside the cold end also limits the conductive heat loads from supports and wiring and the readout dissipation imposed on the cryogenic system [39].

The reference design uses a passive, non-magnetic Bi shield near the TES to attenuate secondary 511-keV photons from activation of the copper cold plate. We evaluated the attenuation using tabulated photon-interaction cross sections [22]. The shield itself contributes delayed activation. Several-MeV atmospheric γ rays can also undergo pair production in the Bi and give rise to annihilation photons.

These local background sources motivate the Lateral-chimney design, which moves the TES beyond the cold-plate projection and places active BGO around the lateral focal plane.

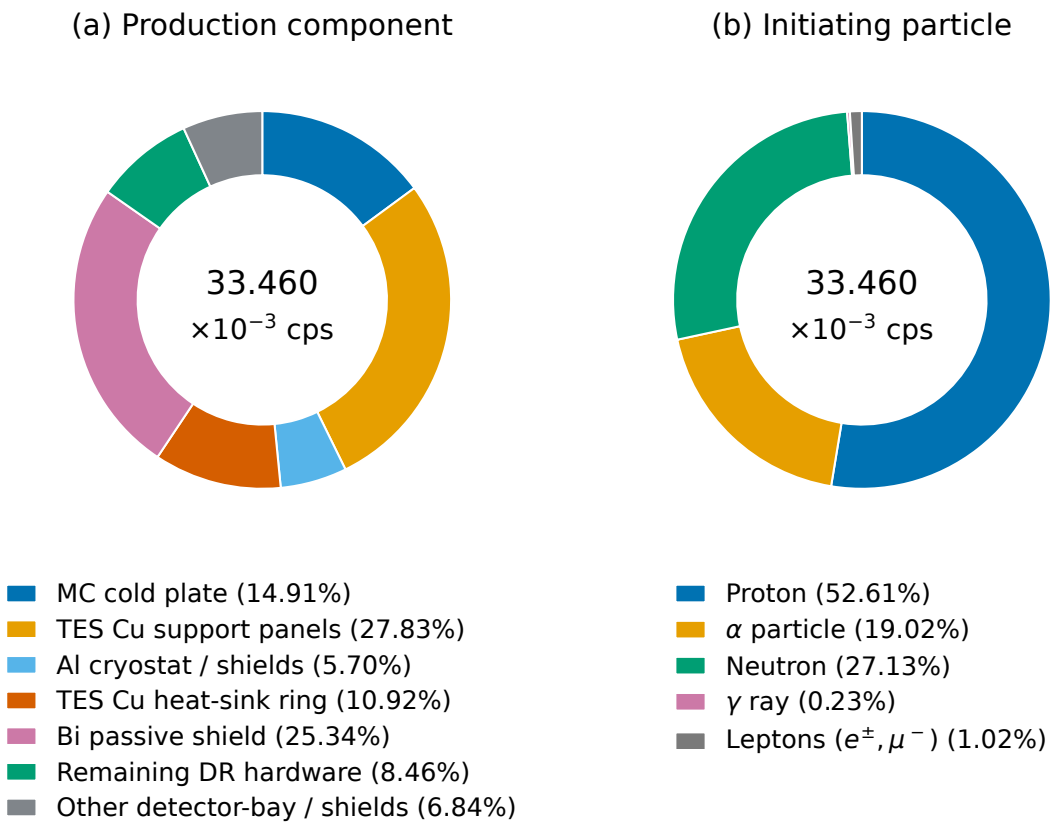

Fig. 7 Origins of the final selected day-15 delayed-activation background in Under-stage. (a) Component in which the parent nuclide was produced. The TES substrate-support copper category combines the support panels; the aluminum cryostat/shield category combines the temperature-stage shield caps, inner shield cylinder, vacuum-jacket cap, and MC aluminum-can bottom cap; "Remaining DR hardware" contains the remaining copper DR/cold-stage parts and the simplified silver-sinter model. The "Other detector-bay / shields" category combines the remaining detector-bay and shielding components. (b) Initiating primary-particle species, with e^+, e^-, and μ^- combined as leptons. Sector areas and legend percentages are normalized to the final delayed-activation rate, $3.346 \times 10^{-2}\,\mathrm{s}^{-1}$

4.3 Lateral-chimney configuration

The Lateral-chimney configuration places the six-layer TES focal plane inside a side chimney rather than directly beneath the staged cold structures, while retaining the copper thermal-support frame of each TES layer. Heat from the layers is collected by the rear copper heat-sink assembly and conducted through a bent copper thermal strap, which passes through a 1.50-cm-diameter rear cold port and connects to the MC cold plate. Except for this thermal-service port, the cold-stage-facing rear face of the focal plane is covered as fully as practicable by an active BGO rear annulus. Together with the chimney-side shield and front optical annulus, it attenuates radiation from the cold-stage direction and vetoes TES candidates when the summed coincident energy in the BGO reaches the veto threshold. Events retain the common $1\,\mu$s time grouping and pass the active selection when the summed BGO deposit in the coincidence cluster is below 50 keV.

The chimney has an outer mechanical jacket, three intermediate shells associated with successive cold stages, and an innermost magnetic shield made of high-purity aluminum. From inside outward, the radial thicknesses of the five aluminum shells are 2, 3, 3, 3, and 5 mm. Their inner/outer radii are 40/42, 44.5/47.5, 50/53, 55.5/58.5, and 61/66 mm, respectively. Each shell includes a side wall, a front optical interface, and a rear cold-service opening. The BGO side shield and front/rear annuli are each 40 mm thick. The front recess is 60 by 60 mm, and the rear cold port has a 7.5 mm radius.

Figure 8 compares the two configurations at the same scale, showing the cold plates, TES, copper thermal straps, and active BGO. Figure 9 shows the Lateral-chimney configuration in an orthographic cutaway.

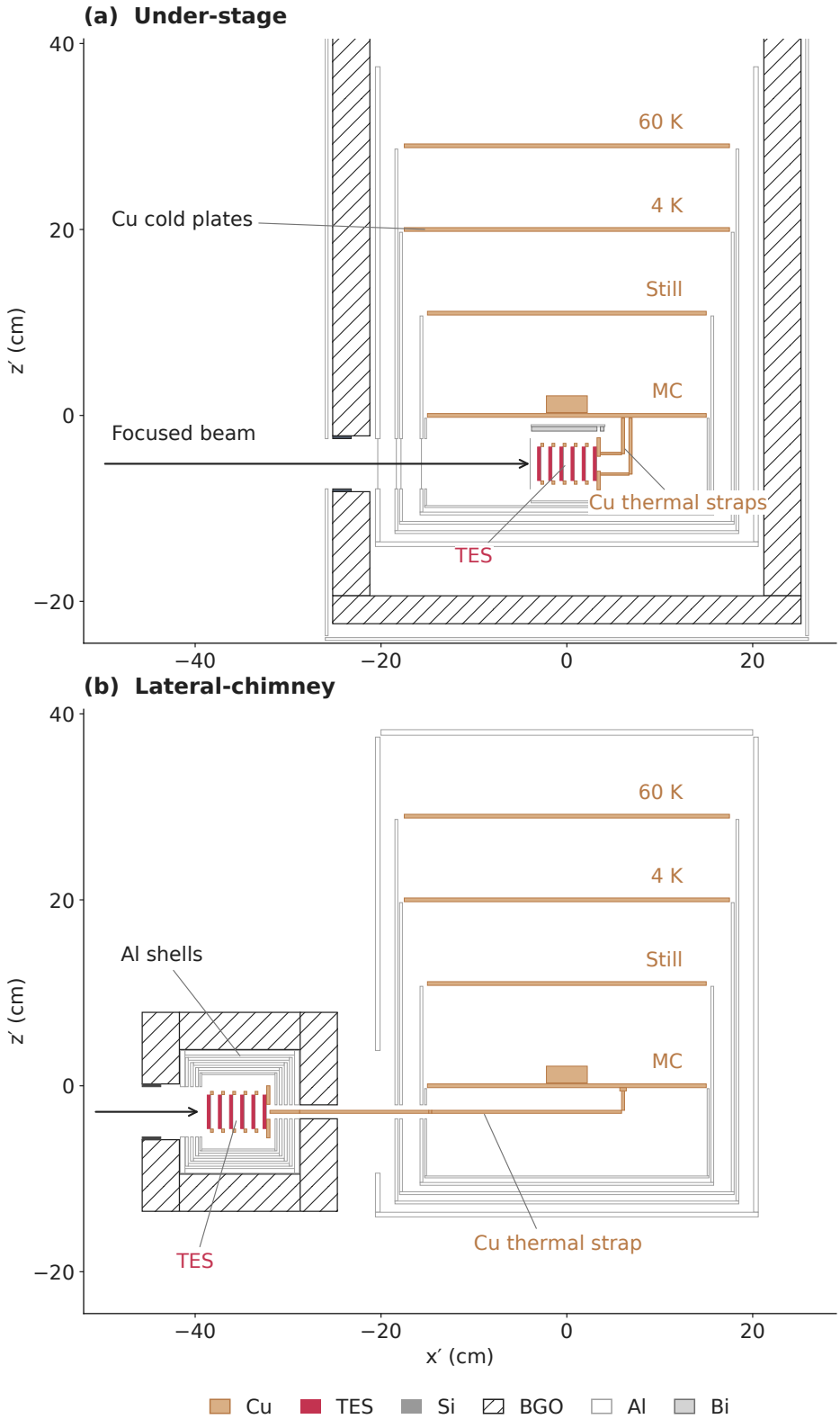

Fig. 8 Functional x'–z' views of (a) Under-stage and (b) Lateral-chimney at the same physical scale. Copper structures and the TES are shown in color; BGO is diagonally hatched, and the remaining structures are shown in gray. Arrows indicate the focused beam. Dense holes in the cold plates and small service details are omitted

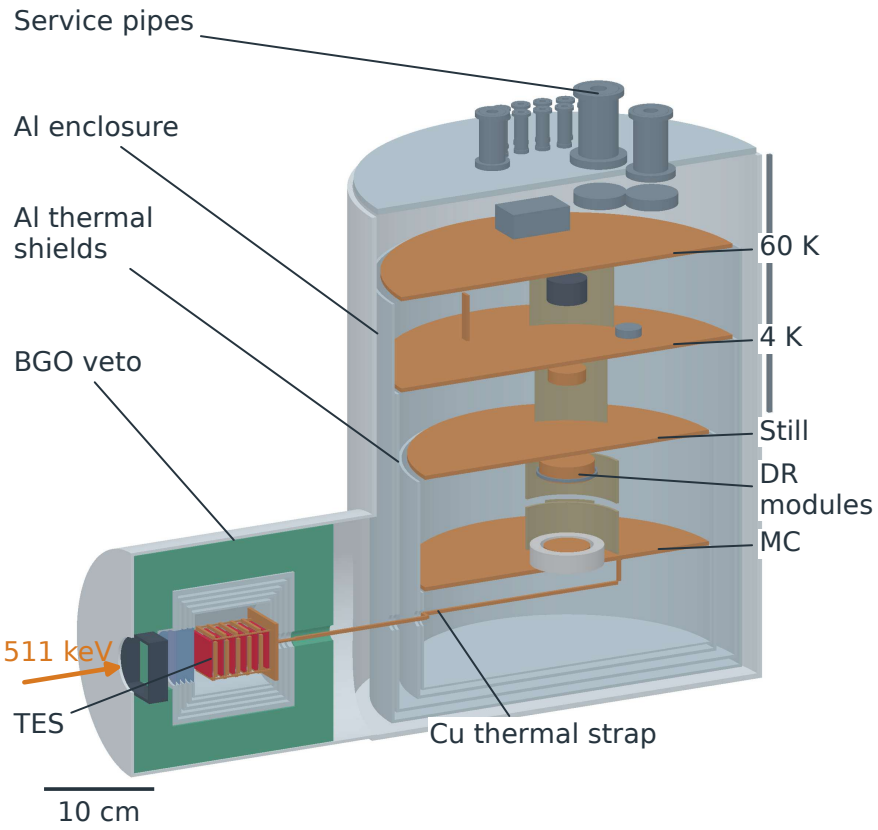

Fig. 9 Orthographic cutaway of the Lateral-chimney configuration, showing the cold plates, DR components, service pipes, lateral focal plane, Al enclosure, BGO, and copper thermal strap connecting the TES to the MC cold plate. The orange arrow indicates the focused 511 keV beam. Dense hole arrays in the cold plates are omitted for clarity

Table 3 summarizes the prompt and delayed transport statistics and their rate normalizations.
Figure 10 shows the production sites for delayed events passing all selections.

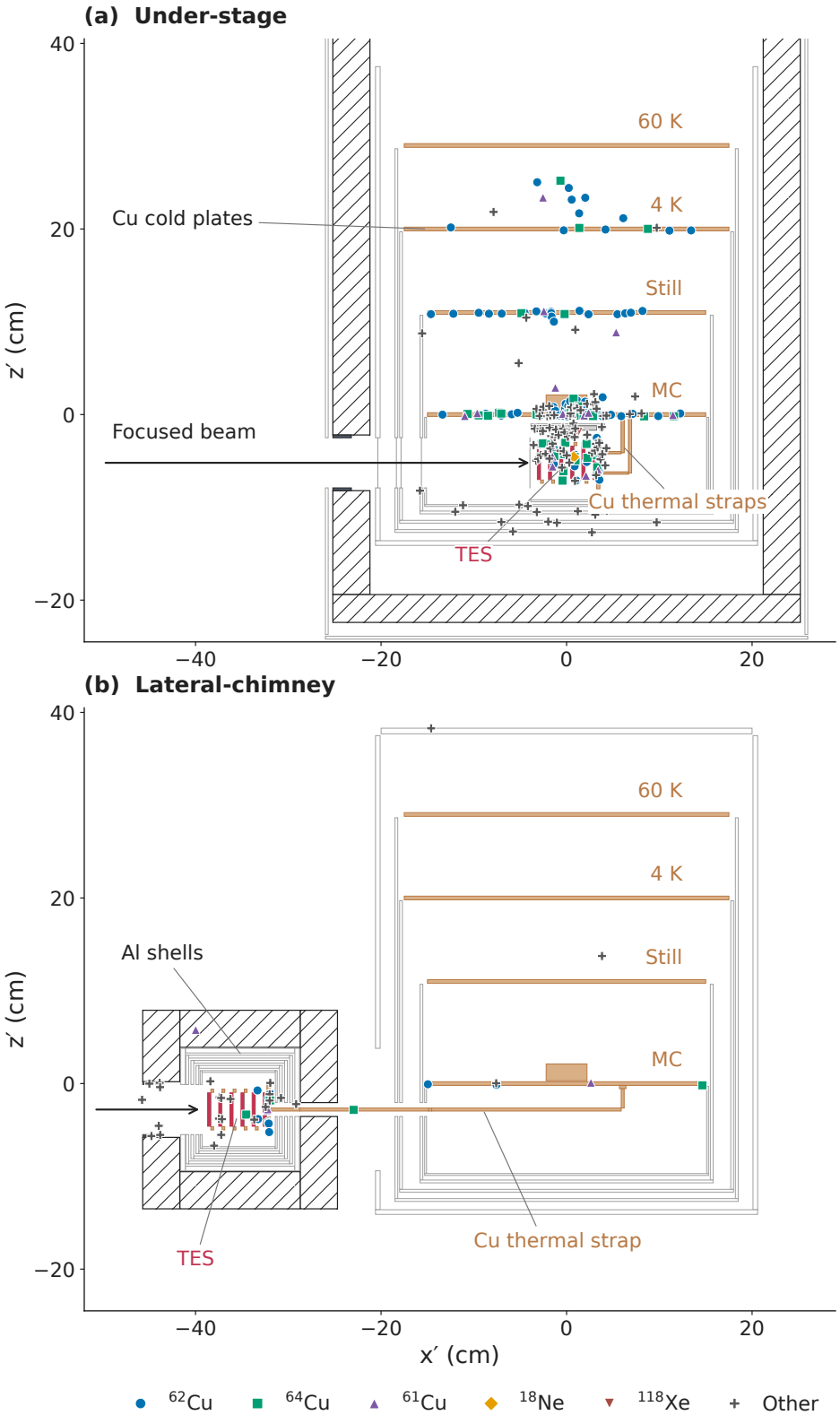

Fig. 10 Production sites of the parent nuclides for selected day-15 delayed events in (a) Under-stage and (b) Lateral-chimney, overlaid on the structures of Figure 8 at the same scale. Symbols identify the five parent nuclides with the largest combined selected rate across both configurations; the remaining nuclides are grouped as Other. Symbol size is fixed, and coincident projected sites within a category are shown once. All events have passed the analysis energy window, active veto, and Compton selection

Table 3: Simulation sample sizes and day-15 physical rates of energy-depositing events. (a) N_{tr} and T_{eq} are the prompt-primary count and equivalent exposure in the reference transport environment. (b) N is the sample size. $N_{\mathrm{det}+}$ counts events with energy deposited in the TES or BGO, with correlated decays combined in panel (b). $R_{\mathrm{cat},15}$ is their physical rate at mission day 15.

(a) Prompt atmospheric-particle transport

Model	Species	N_{tr}	T_{eq} (s)	$N_{\mathrm{det}+}$	$R_{\mathrm{cat},15}$ (s^{-1})
Under-stage	γ	112,419,018	2071	30,856,570	1.368×10^{4}
	n	8,358,073	1599	2,160,853	1311
	e^{-}	3,598,197	1599	746,558	452.7
	e^{+}	2,118,782	1601	662,267	399.9
	p	2,033,775	1603	639,070	388.9
	α	207,881	1608	67,649	42.95
	μ^{-}	90,447	1608	29,046	16.56
	μ^{+}	101,230	1613	32,375	18.40
Lateral-chimney	γ	112,421,262	2071	4,189,660	1856
	n	8,363,786	1599	325,382	197.4
	e^{-}	3,602,914	1599	136,738	82.92
	e^{+}	2,119,548	1601	139,963	84.51
	p	2,036,710	1603	123,624	75.23
	α	209,074	1608	18,285	11.61
	μ^{-}	91,020	1608	4,605	2.626
	μ^{+}	102,306	1613	5,268	2.994

(b) Delayed-decay transport at day 15

Model	Species	N	$N_{\mathrm{det}+}$	$R_{\mathrm{cat},15}$ (s^{-1})
Under-stage	γ	1,000,000	837,986	6.586
	n	1,000,000	683,598	437.4
	e^{-}	1,000,000	606,881	0.699
	e^{+}	1,000,000	630,745	4.166
	p	1,000,000	705,783	998.2
	α	1,000,000	696,567	363.8
	μ^{-}	1,000,000	685,132	0.2698
	μ^{+}	1,000,000	1,000,000	2.150×10^{-3}
Lateral-chimney	γ	1,000,000	369,939	0.9222
	n	1,000,000	573,901	57.41
	e^{-}	1,000,000	414,020	0.1276
	e^{+}	1,000,000	487,291	0.4075
	p	1,000,000	880,244	124.6
	α	1,000,000	679,868	39.51
	μ^{-}	1,000,000	403,787	3.281×10^{-2}
	μ^{+}	1,000,000	1,867	6.828×10^{-6}

4.4 Selected backgrounds and their origins in Lateral-chimney

Table 4 summarizes the day-15 selection results for Lateral-chimney by background component, showing the suppression achieved by the active veto and Compton selection. The final row gives the total background rate including accidental coincidences on the common Poisson timeline, providing the day-15 input to the sensitivity calculation.

In the isolated-event results, active BGO reduces the total background rate from $2.458\,\mathrm{s}^{-1}$ (7,908 simulated events) to $1.248 \times 10^{-2}\,\mathrm{s}^{-1}$ (156 events), or 0.5077% of the pre-veto rate. All 28,568 isolated focused-signal events in the measured energy window pass the active selection. The subsequent Compton event selection leaves 149 background events and retains 96.87% of the active-veto weighted background rate.

For the focused signal, the Compton selection retains 28,000 of those 28,568 events, a retention fraction of 98.01%.

The final Lateral-chimney isolated-event background contains $1.811 \times 10^{-3}\,\mathrm{s}^{-1}$ from the seven non-γ prompt particle species, $5.863 \times 10^{-3}\,\mathrm{s}^{-1}$ from atmospheric γ rays, and $4.412 \times 10^{-3}\,\mathrm{s}^{-1}$ from delayed activation. Their shares are 14.99%, 48.51%, and 36.50%, respectively. Relative to Under-stage, the delayed and atmospheric-γ rates fall to 13.2% and 37.79%, and the total rate is $1.209 \times 10^{-2}\,\mathrm{s}^{-1}$, or 24.38% of the Under-stage value, a factor of 4.10 lower. Table 5 lists the component rates and Monte Carlo standard errors.

Copper-derived events contribute $(2.73 \pm 0.53) \times 10^{-3}\,\mathrm{s}^{-1}$, or 61.97% of the final Lateral-chimney delayed rate. The

Table 4: Day-15 Lateral-chimney selection at 500 eV FWHM. The isolated-event background entries give simulated event counts and weighted rates; the signal entries give counts and retention relative to the signal in the analysis energy window before active anticoincidence. The Poisson-timeline row gives selected background clusters and rates from the Poisson simulation with 2×10^5 s exposure.

Stream	Pre-veto	After active veto	Final selection
Isolated-event results			
Non-γ prompt	1452 / $0.8811\,\mathrm{s}^{-1}$	3 / $1.811 \times 10^{-3}\,\mathrm{s}^{-1}$	3 / $1.811 \times 10^{-3}\,\mathrm{s}^{-1}$
Atmospheric γ	2996 / $1.383\,\mathrm{s}^{-1}$	14 / $5.863 \times 10^{-3}\,\mathrm{s}^{-1}$	14 / $5.863 \times 10^{-3}\,\mathrm{s}^{-1}$
Delayed activation	3460 / $0.1933\,\mathrm{s}^{-1}$	139 / $4.802 \times 10^{-3}\,\mathrm{s}^{-1}$	132 / $4.412 \times 10^{-3}\,\mathrm{s}^{-1}$
Total background	7908 / $2.458\,\mathrm{s}^{-1}$	156 / $1.248 \times 10^{-2}\,\mathrm{s}^{-1}$	149 / $1.209 \times 10^{-2}\,\mathrm{s}^{-1}$
Focused signal	28568 / 100%	28568 / 100%	28000 / 98.01%
Common Poisson timeline			
Total background	491354 / $2.457\,\mathrm{s}^{-1}$	2388 / $1.194 \times 10^{-2}\,\mathrm{s}^{-1}$	2320 / $1.160 \times 10^{-2}\,\mathrm{s}^{-1}$

Table 5: Day-15 final isolated-event background of Lateral-chimney at 500 eV FWHM. Standard errors and effective sample sizes use $\sum_i w_i^2$.

Component	Events	Rate / cps	Error / cps	N_{eff}	Share / %
Non-γ prompt	3	1.811×10^{-3}	1.046×10^{-3}	3.00	14.99
Atmospheric γ	14	5.863×10^{-3}	1.598×10^{-3}	13.47	48.51
Delayed activation	132	4.412×10^{-3}	6.575×10^{-4}	45.03	36.50
Total	149	1.209×10^{-2}	2.020×10^{-3}	35.82	100.00

spatial-region contribution from the DR/mixing chamber and staged cold plates falls from $(0.67 \pm 0.07) \times 10^{-2}\,\mathrm{s}^{-1}$ in Under-stage to $(1.8 \pm 1.4) \times 10^{-4}\,\mathrm{s}^{-1}$ in Lateral-chimney. The total delayed rate changes from $(3.35 \pm 0.15) \times 10^{-2}$ to $(4.41 \pm 0.66) \times 10^{-3}\,\mathrm{s}^{-1}$.

The TES Cu support panels and heat-sink ring together account for 52.13% of the residual delayed rate, while the MC cold plate contributes 4.09%. Protons are the leading initiating particles (53.57%; Figure 11).

When grouped by parent nuclide, ^{62}Cu is the largest single delayed-background contributor in both mass models. Its weighted rate is $1.339 \times 10^{-2}\,\mathrm{s}^{-1}$ in Under-stage and $1.519 \times 10^{-3}\,\mathrm{s}^{-1}$ in Lateral-chimney, accounting for 40.00% and 34.43% of the respective final delayed rates. Together, ^{61}Cu, ^{62}Cu, and ^{64}Cu contribute 55.70% of the final delayed rate in Under-stage and 50.14% in Lateral-chimney. Figure 12 compares the leading parent-nuclide compositions.

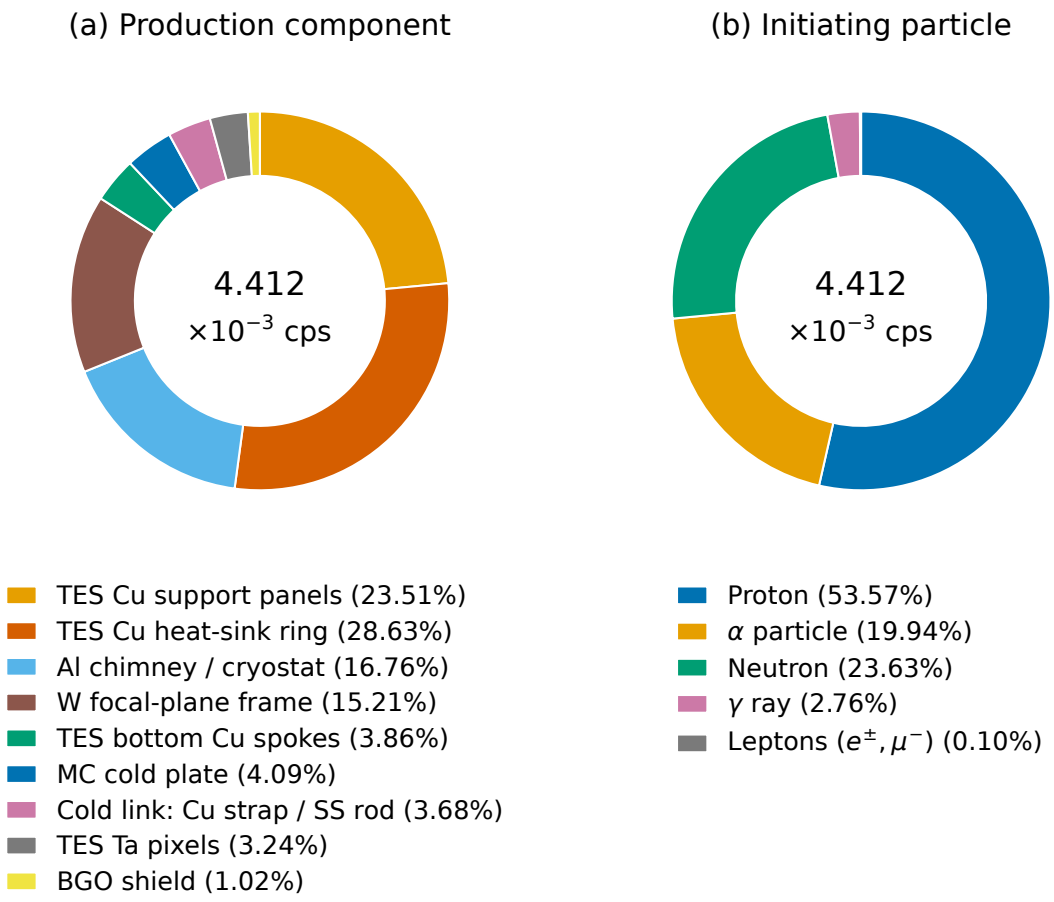

Fig. 11 Origins of the final day-15 delayed-activation background in Lateral-chimney. (a) Component in which the parent nuclide was produced. (b) Primary particle that initiated its production. Four Cu substrate-support panels are grouped, as are the Al chimney/port/lid/annulus volumes and the Cu-strap/SS-rod cold link; Ta pixels and BGO remain separate. Leptons combine e^-, e^+, and μ^-. Both panels use $4.412 \times 10^{-3}\,\mathrm{s}^{-1}$ as their denominator

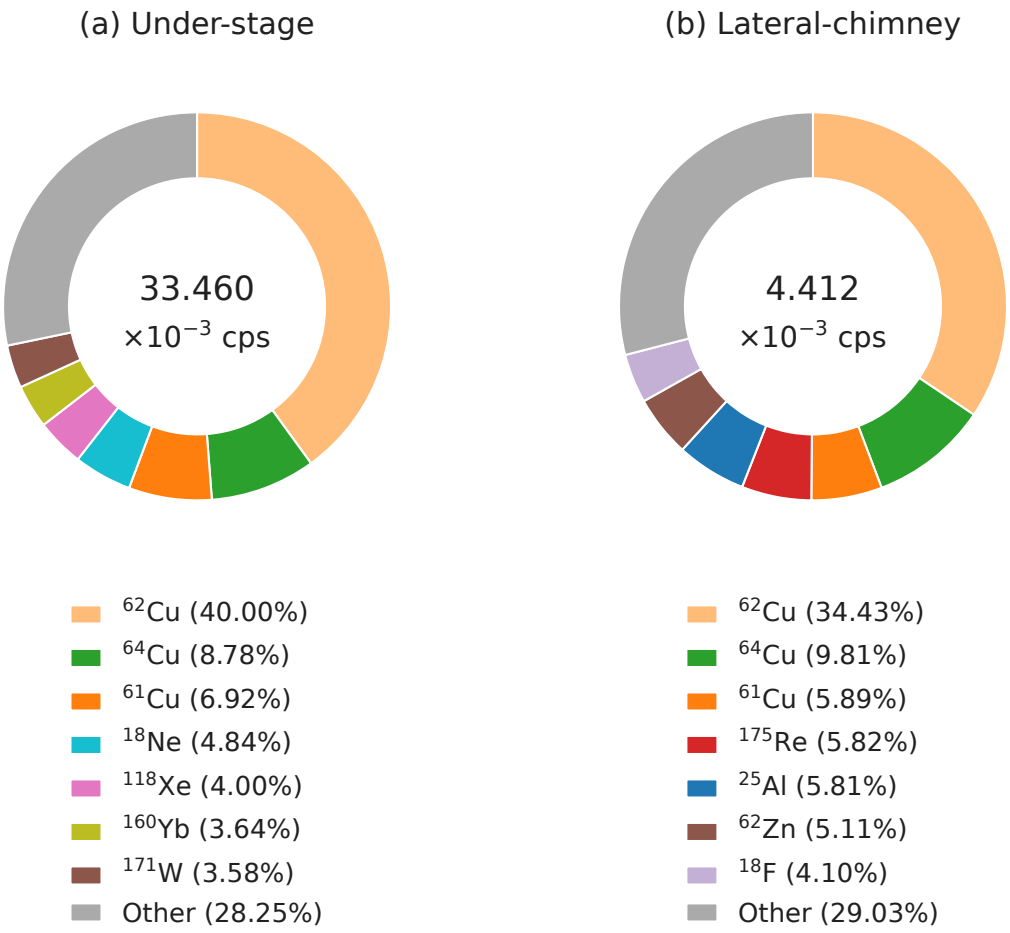

Fig. 12 Composition by parent nuclide of the final selected day-15 delayed-activation background in (a) Under-stage and (b) Lateral-chimney. Sector area gives each parent nuclide's fraction of the corresponding final delayed rate. The seven leading parent nuclides are shown separately in each panel and the remainder is grouped as Other. Nuclides shared by the two panels use the same colors, and the total delayed-background rate is printed at each center. Contributions include selected decays of the descendants of each parent nuclide

Figure 13 compares the final fractional compositions of the two models using the same categories.

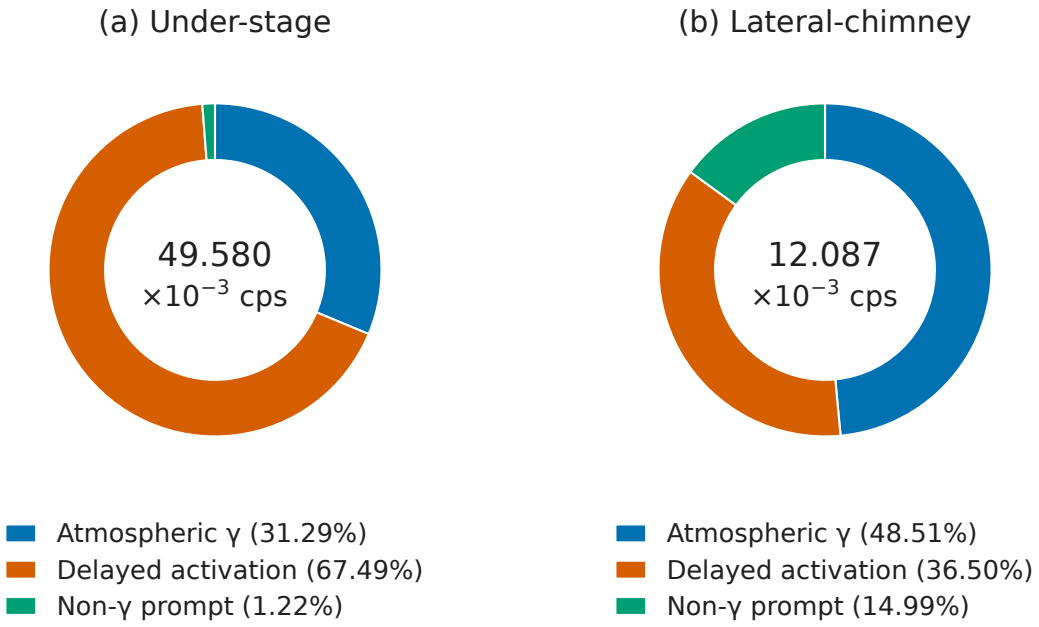

Fig. 13 Composition of the final isolated-event background in the day-15 510.50–$511.50\,\mathrm{keV}$ analysis energy window after all selections. Sector area gives each physical component's fraction of the corresponding model total, shown at the center; the same component colors are used in both panels

Figure 14 shows the day-15 background spectra near 511 keV before active anticoincidence, after active selection, and after the final Compton selection.

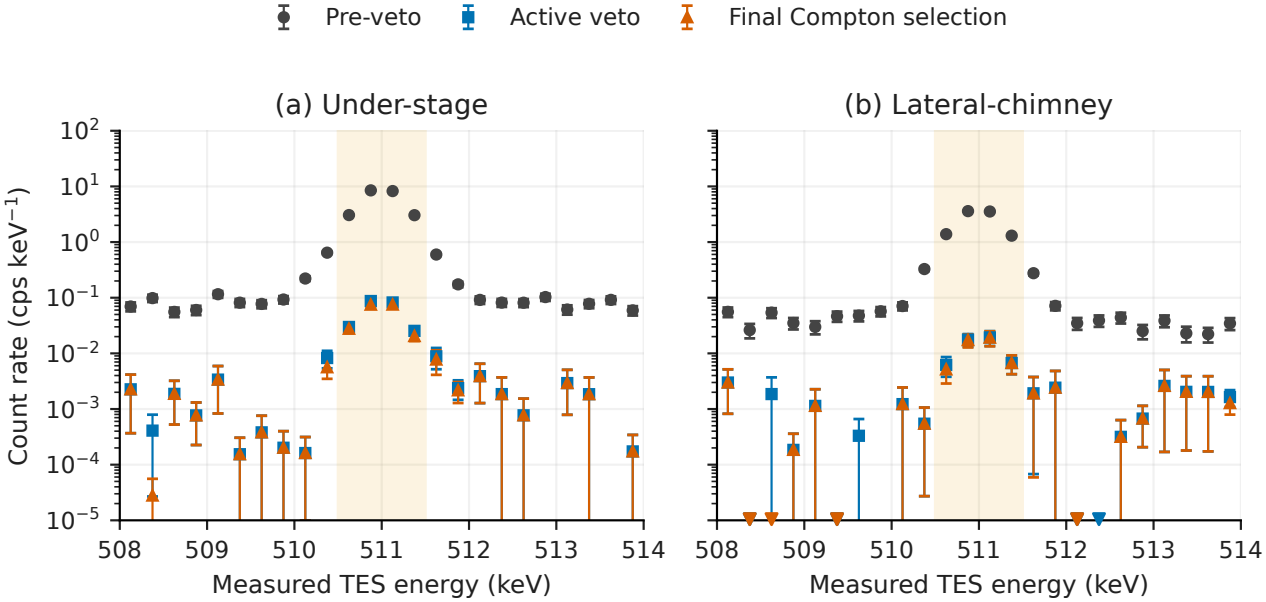

Fig. 14 Day-15 detector-background spectra near 511 keV for (a) Under-stage and (b) Lateral-chimney, using 0.25 keV bins. The shaded interval marks the $[510.50, 511.50)\,\mathrm{keV}$ analysis energy window. Symbols show the isolated-event background before active anticoincidence, after active anticoincidence, and after the final Compton event selection. Error bars show Monte Carlo 1σ uncertainties from $\sqrt{\sum_i w_i^2}$; zero-weight bins are blank. Downward triangles at the lower plotting limit mark positive rates below the displayed range; error bars extending below that limit are clipped

Delayed activation accounts for 67.5% of the selected day-15 isolated-event background in Under-stage. In Lateral-chimney, the two largest estimated contributions are atmospheric γ rays (48.5%) and delayed activation (36.5%).

4.5 Time-domain simulation and cumulative counts

The simulation at each sampled time uses an equivalent exposure of 2×10^5 s for both configurations.

Figure 15 compares the simulated background rates at days 0, 5, 10, 15, and 20 with the analytic curves. Differences between the simulated rates and the analytic curves arise from accidental-coincidence selection effects and Poisson sampling fluctuations. The event-time simulations sample from the component rates defined in Equations (12)–(15).

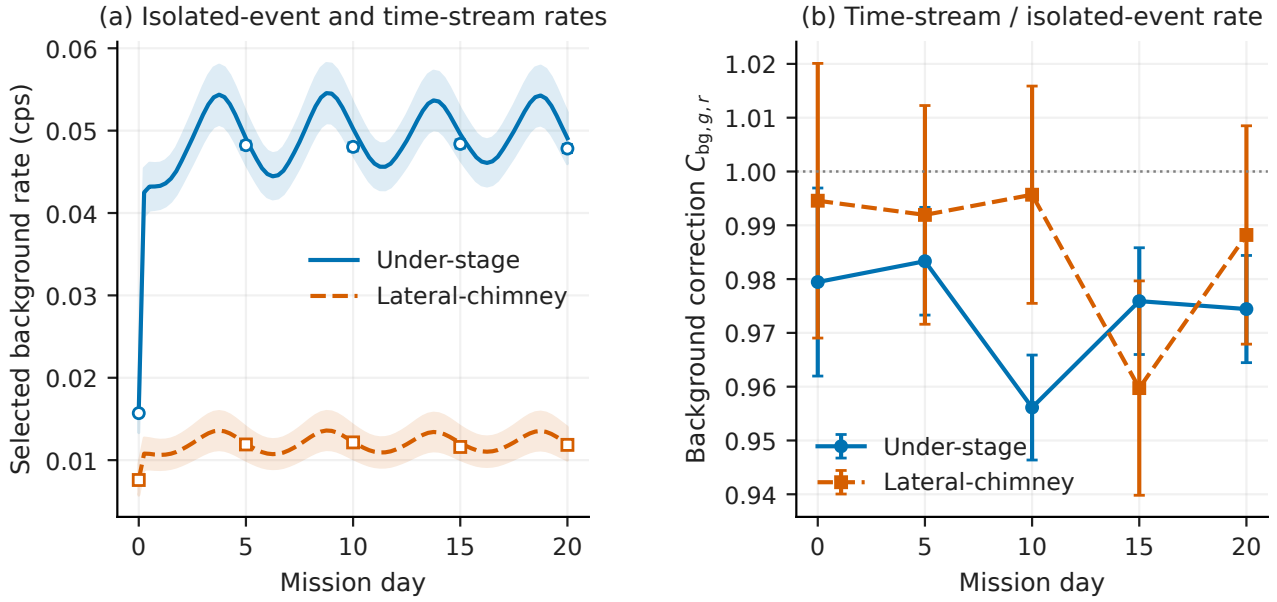

Fig. 15 Comparison of isolated-event estimates and time-stream simulations. (a) Curves show analytic rates for individually selected events; open symbols show simulated rates after Poisson time-stream superposition, with an equivalent exposure of 2×10^5 s per point. Shaded bands and error bars show the transport-template 1σ uncertainties and Poisson sampling errors, respectively. (b) Simulated-to-analytic rate ratios; the horizontal line marks unity, and error bars include only Poisson sampling errors

At days 0, 5, 10, 15, and 20, the ratio of the final background rate from the event-time simulation to the isolated-event rate estimates the background coincidence correction factor $C_{\mathrm{bg},g}$. The sampled $C_{\mathrm{bg},g}$ values span 0.9561–0.9833 for Under-stage and 0.9597–0.9957 for Lateral-chimney (Figure 15).

At the reference flux defined in Section 3.4, the day-15 final signal rates are 1.763×10^{-3} and $1.806 \times 10^{-3}\,\mathrm{s}^{-1}$ for Under-stage and Lateral-chimney, respectively.

At 20 d, the expected signal/background counts are 2976/82,573 for Under-stage and 3122/20,534 for Lateral-chimney. Atmospheric γ rays and the remaining background contribute 26,404/56,169 counts in Under-stage and 10,098/10,436 in Lateral-chimney. The Lateral-chimney cumulative background is 24.87% of the Under-stage value.

4.6 Mission significance and minimum detectable line flux

Figure 16 and Table 6 summarize the mission performance. At F_{ref}, the 20 d counting significances are 10.36 for Under-stage and 21.79 for Lateral-chimney. The corresponding 3σ minimum detectable top-of-atmosphere fluxes are $(6.95 \pm 0.23) \times 10^{-5}$ and $(3.30 \pm 0.28) \times 10^{-5}\,\mathrm{ph\,cm^{-2}\,s^{-1}}$.

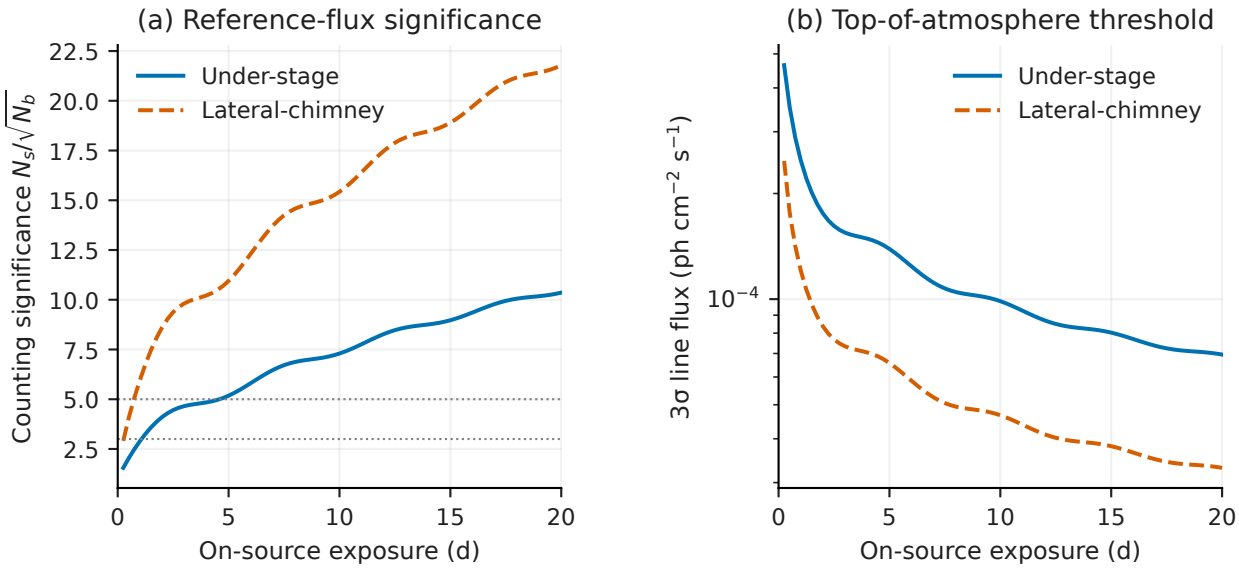

Fig. 16 Projected mission performance of the Under-stage and Lateral-chimney configurations. (a) Counting significance at the top-of-atmosphere reference flux $F_{\rm ref} = 2.4\times10^{-4}\,\mathrm{ph\,cm^{-2}\,s^{-1}}$; horizontal lines mark 3σ and 5σ. (b) Corresponding 3σ minimum detectable top-of-atmosphere flux.

Table 6: Projected performance for a 20 d on-source observation at 500 eV FWHM.

Quantity	Under-stage	Lateral-chimney
Day-15 isolated-event background / cps	4.958×10^{-2}	1.209×10^{-2}
Day-15 signal at $F_{\rm ref}$ / cps	1.763×10^{-3}	1.806×10^{-3}
20 d background counts	82573	20534
20 d signal counts at $F_{\rm ref}$	2976	3122
$Z_{20\mathrm{d}} = N_s/\sqrt{N_b}$	10.36	21.79
$T_{3\sigma}$ at $F_{\rm ref}$ / d	1.07	0.27
$T_{5\sigma}$ at $F_{\rm ref}$ / d	4.58	0.73
$F_{3\sigma}(20\,\mathrm{d})$ / $\mathrm{ph\,cm^{-2}\,s^{-1}}$	$(6.95 \pm 0.23) \times 10^{-5}$	$(3.30 \pm 0.28) \times 10^{-5}$
$F_{5\sigma}(20\,\mathrm{d})$ / $\mathrm{ph\,cm^{-2}\,s^{-1}}$	$(11.59 \pm 0.38) \times 10^{-5}$	$(5.51 \pm 0.47) \times 10^{-5}$

At the same reference flux, the 20 d Lateral-chimney background and signal counts are 24.87% and 1.049 times the Under-stage values, respectively. The flux-threshold ratio is therefore:

$$\frac{F_{\mathrm{min,Under\text{-}stage}}}{F_{\mathrm{min,Lateral\text{-}chimney}}} = \sqrt{\frac{N_{b,\mathrm{Under\text{-}stage}}}{N_{b,\mathrm{Lateral\text{-}chimney}}}}\,\frac{N_{s,\mathrm{Lateral\text{-}chimney}}}{N_{s,\mathrm{Under\text{-}stage}}} \simeq 2.005 \times 1.049 \simeq 2.104. \tag{22}$$

Equation (22) shows that most of the 2.10-fold threshold difference follows from the square root of the background-count ratio, with a smaller contribution from the higher signal count.

5 Estimated response in different radiation environments

The balloon calculation establishes the Lateral-chimney response and trajectory-integrated sensitivity. To identify which radiation fields would limit the same detector response in other mission environments, we traced the selected events back to their primary particle types and energies and reweighted them with source spectra for an Antarctic balloon location, LEO, the lunar surface, and Sun–Earth L2. The reweighting changes the source spectra while retaining the balloon angular-response and day-15 activation templates. The calculation therefore shows how a change in radiation environment acts on the established TES response and helps set priorities for detailed follow-up simulations.

5.1 Spectral reweighting

We considered five alternative source fields. For an Antarctic balloon flight, EXPACS/PARMA [31, 32] provides the spectra at a representative location of 77.85° S, 166.67° E. The source altitude of 38 km and solar-activity index $W = 118.3$ match the reference balloon inputs; the adopted geomagnetic cutoff rigidity changes from 11.6 GV to approximately zero. The Antarctic spectra are generated using the same source model as for the reference environment.

The four space environments are quiet, near-equatorial LEO at 530 km outside the SAA, an exposed lunar surface, and Sun–Earth L2 at solar maximum and solar minimum. Sun–Earth L2 is also considered for its favorable thermal environment for cryogenic TES operation. The LEO spectra use the components adopted in low-Earth-orbit gamma-ray background studies [33]. The lunar field combines the upward REDMoon spectrum for Apollo-17 regolith with the cosmic gamma-ray sky visible from the surface [40]. The L2 fields contain gamma rays, protons, alpha particles, electrons, and positrons, with GCR spectra appropriate to the two solar-modulation conditions [41–43].

For the prompt-gamma background, each selected event retains the energy of its primary photon. A selected delayed event is linked instead to the activation-production energy distribution for the same incident particle, parent nuclide, and production region. At those primary energies, each balloon event weight is multiplied by the ratio of the target spectrum to the balloon spectrum. The spectral ratios are evaluated for all events selected with the 500 eV response and weighted by their day-15 event rates. The day-15 rate-weighted 10th–90th percentile bands of the primary-energy distributions shown in Figure 17 are 0.515–29.5 MeV for selected prompt gamma rays and 1.37–51.3 GeV for proton-induced delayed background.

The seven non-gamma prompt species contribute 15.0% of the balloon background. All three surviving events have positron primaries. Because an independent energy-dependent response for prompt positrons is unavailable, their aggregate rate follows the combined prompt-gamma and delayed-activation scaling; no species-resolved target-environment rates are reported.

All scenarios use the same 20 d exposure, optical response, and Lateral-chimney signal-retention fraction. The estimated minimum detectable line flux is anchored to the balloon result of $3.30 \times 10^{-5}\,\mathrm{ph\,cm^{-2}\,s^{-1}}$ and scales with the square root of the reweighted background. The Antarctic estimate retains the reference altitude history and fixed 27° source elevation, so both balloon cases have the same atmospheric transmission. For the space environments, the cumulative signal loss from the balloon atmosphere and observing trajectory is removed. The balloon values are quoted at the top of the atmosphere; the LEO, lunar-surface, and L2 values refer to the local instrument incident plane.

5.2 Estimated backgrounds and sensitivities

Table 7: Spectral-reweighting estimates for Lateral-chimney in different radiation environments. The third column gives the combined prompt-gamma and delayed-activation rate relative to the balloon reference. For the other environments, we estimate the flux thresholds by reweighting the reference balloon background events using the corresponding source spectra.

Scenario	Adopted radiation field	Background/ balloon	20 d 3σ flux ($\mathrm{ph\,cm^{-2}\,s^{-1}}$)
Balloon reference	reference trajectory	1.00	3.30×10^{-5}
Antarctic balloon	77.85° S, 166.67° E, 38 km	3.53	6.21×10^{-5}
530 km LEO	near-equatorial, quiet non-SAA	0.568	1.27×10^{-5}
Exposed lunar surface	REDMoon Apollo-17 regolith	23.3	8.13×10^{-5}
Sun–Earth L2 (2014)	solar maximum, GCR-low	6.34	4.24×10^{-5}
Sun–Earth L2 (2009)	solar minimum, GCR-high	12.7	6.01×10^{-5}

For the Antarctic reference spectrum, the selected prompt-gamma and delayed background rates are $9.73 \times 10^{-3}\,\mathrm{s^{-1}}$ and $2.66 \times 10^{-2}\,\mathrm{s^{-1}}$, respectively. Their sum is 3.53 times the reference balloon value, giving a 20 d estimated minimum detectable line flux of $6.21 \times 10^{-5}\,\mathrm{ph\,cm^{-2}\,s^{-1}}$ under the same altitude and elevation assumptions. The lower geomagnetic cutoff increases the particle background, particularly activation.

At this Antarctic latitude, the Galactic center remains above the horizon, with elevations of approximately 17°–41°. At upper culmination and the reference day-15 atmospheric column, the 511-keV transmission reaches 0.632, compared with 0.514 at 27°. The transmission gain over a flight depends on the altitude and elevation history.

For quiet non-SAA LEO, the reweighted background is 0.568 times the balloon reference. After removing the signal loss associated with the balloon atmosphere and observing trajectory, the 20 d estimated minimum detectable line flux is $1.27 \times 10^{-5}\,\mathrm{ph\,cm^{-2}\,s^{-1}}$. Thus, in quiet orbital segments, the current source field produces less background in Lateral-chimney than the balloon environment. For a 550 km equatorial orbit, Cumani et al. estimated that the region occupied by trapped particles above 0.1 MeV accounts for about 18% of the orbital period [33]. The 20 d value in Table 7 denotes live science exposure. The next LEO calculation should concentrate on activation by SAA and trapped particles and on the delayed background after an SAA passage.

For the exposed lunar surface, the reweighted background rises to 23.3 times the balloon reference and the estimated

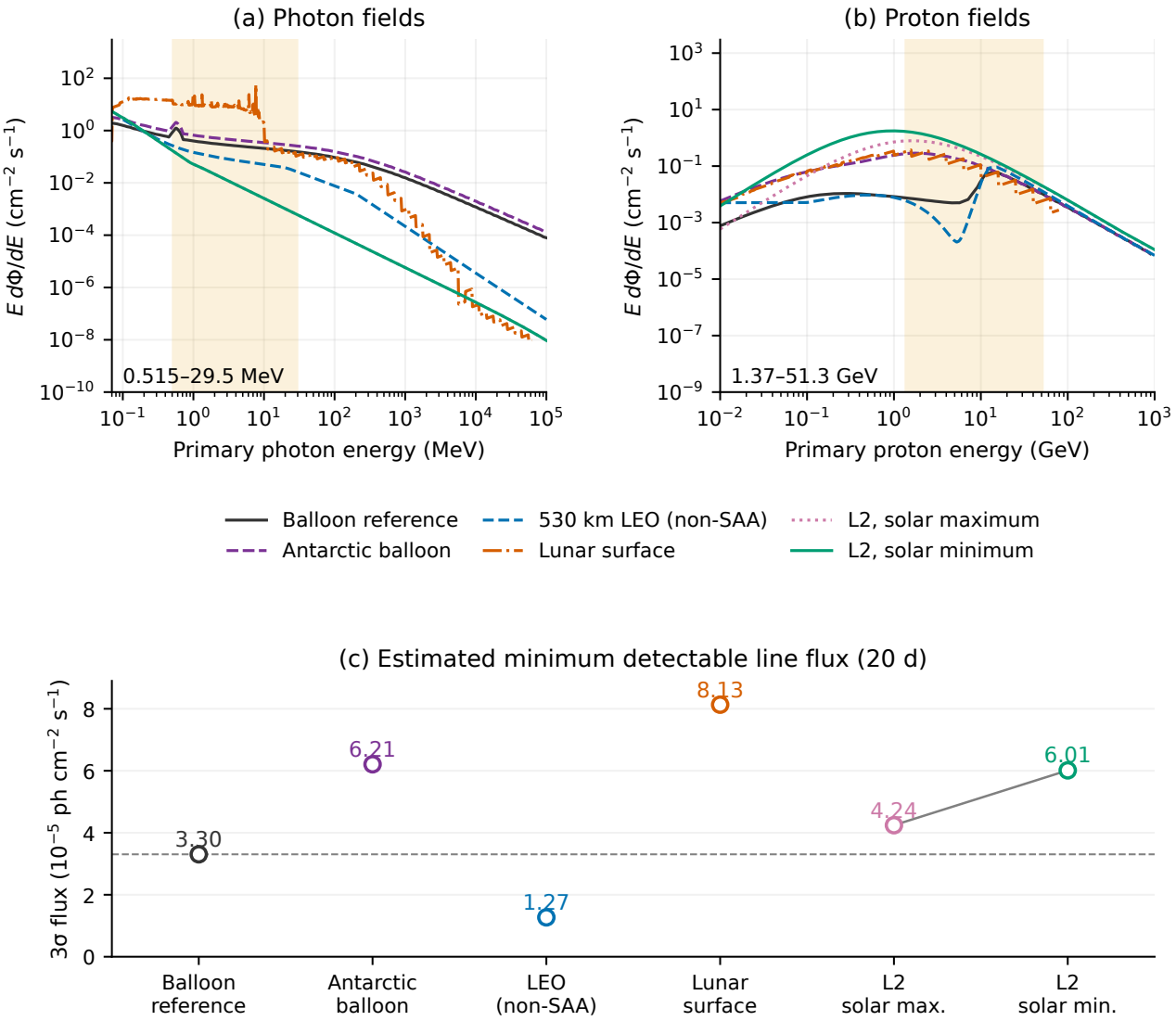

Fig. 17 Environmental spectral reweighting for Lateral-chimney. (a) Gamma-ray source spectra; the shaded band is the principal primary-energy range of the selected prompt-gamma events (0.515–29.5 MeV). (b) Proton spectra; the shaded band is the principal response range of the proton-induced delayed background (1.37–51.3 GeV). The shaded bands span the day-15 rate-weighted 10th–90th percentiles of the primary-energy distributions. (c) The 20 d, 3σ estimated minimum detectable line flux anchored to the reference balloon result. Both balloon estimates refer to the top of the atmosphere. The space-environment values refer to the local instrument incident plane

minimum detectable line flux becomes $8.13 \times 10^{-5}\,\mathrm{ph\,cm^{-2}\,s^{-1}}$. The increase is driven mainly by upward regolith radiation in the response band of the selected gamma-ray events. A lunar application therefore requires a local gamma-ray field that couples the regolith, detector, and lander structure rather than an isolated-payload model.

At Sun–Earth L2, the result follows solar modulation. The 2014 solar-maximum/GCR-low field gives $4.24 \times 10^{-5}\,\mathrm{ph\,cm^{-2}\,s^{-1}}$, whereas the 2009 solar-minimum/GCR-high field gives $6.01 \times 10^{-5}\,\mathrm{ph\,cm^{-2}\,s^{-1}}$. Their ordering tracks the proton spectra and identifies GCR-proton activation as the dominant source of the activation background at L2.

6 Summary

The day-15 isolated-event background rate of Under-stage is $4.958 \times 10^{-2}\,\mathrm{s^{-1}}$, with delayed activation as the largest component. Independent spatial and material projections assign 20.03% of the delayed rate to the DR mixing chamber and staged cold region and 59.47% to copper, respectively. The leading structures are the MC cold plate, the TES substrate-support copper panels, and the TES copper heat-sink ring. The analysis-window background is governed by the distance, direct lines of sight, and shield coverage between activated material and the TES.

Lateral-chimney places the six TES layers laterally in a BGO-surrounded chimney. Its day-15 isolated-event back-

ground rate is $1.209 \times 10^{-2}\,\mathrm{s}^{-1}$, composed of 48.51% atmospheric gamma rays, 36.50% delayed activation, and 14.99% from the seven non-gamma prompt species. Including the accidental-coincidence correction, its 20 d, top-of-atmosphere 3σ minimum detectable line flux is $(3.30 \pm 0.28) \times 10^{-5}\,\mathrm{ph\,cm^{-2}\,s^{-1}}$, a factor of 2.10 lower than for Under-stage.

The results support two priorities: reduce coupling between the TES and activation-prone structures near the TES by reducing or relocating them and blocking direct lines of sight, and increase active-BGO coverage around the TES while preserving the focused-beam entrance. In Lateral-chimney, the TES substrate-support copper panels and copper heat-sink ring still account for 52.13% of the residual delayed background and are the direct targets for redesign of the structures nearest the TES.

7 Future work

A further detector-level study should address neutron elastic scattering in the cryogenic Si wafer and nearby focal-plane supports. Nuclear-recoil energy deposited in these volumes can generate athermal and thermal phonons; if a fraction couples to the TES, the response may appear as a non-photon pulse or as thermal cross-talk [44, 45]. Coupled neutron-transport, substrate-phonon, TES thermal-network, and measured pulse-template studies, together with neutron-beam calibration, are needed to determine whether such events can be reconstructed in the 511 keV analysis energy window and whether their pulse shapes permit rejection.

Statements and Declarations

Author contributions Haoyu Li: methodology, analysis, validation, visualization, and writing. Jiangzhen Hong, Congzhan Liu, and Yifei Zhang: provision of the TES model. Weichun Jiang and Ming Li: Laue-lens design. Jia Quan and Lingjiao Wei: initial design of the cryogenic refrigerator. Jianghua Zhou and Rongchen Zhu: balloon design. He Gao and Zhengwei Li: TES readout scheme. Daikang Yan, Wenxi Peng, Xilu Wang, Dongya Guo, and Hua Feng: conceptualization, supervision, writing and reviewing. Except for the first author and the first corresponding author, all co-authors are listed in alphabetical order by surname.

Funding This work was supported by the National Natural Science Foundation of China under Grant 12305209.

Competing interests The authors declare no competing interests.

Data and code availability The data and analysis code supporting the findings of this study are available from the corresponding author upon reasonable request.

Ethics approval and consent to participate Not applicable.

Use of AI and AI-Assisted Technologies During the preparation of this work, the authors used OpenAI Codex and ChatGPT to assist with code development and debugging as well as for language editing and consistency checks of the manuscript. All core methodologies, physical models, and computational algorithms were independently designed and implemented by the authors. The authors reviewed and verified all AI-assisted code and text, and take full responsibility for the methodology, results, and conclusions reported in this work.

References

[1] N. Prantzos, C. Boehm, A.M. Bykov, R. Diehl, K. Ferriere, N. Guessoum, P. Jean, J. Knoedlseder, A. Marcowith, I.V. Moskalenko, A. Strong, G. Weidenspointner, The 511 keV emission from positron annihilation in the Galaxy, Rev. Mod. Phys. 83 (2011) 1001–1056, https://doi.org/10.1103/RevModPhys.83.1001.

[2] P. Jean, J. Knodlseder, W. Gillard, N. Guessoum, K. Ferrière, A. Marcowith, V. Lonjou, J. P. Roques, Spectral analysis of the Galactic e^+e^- annihilation emission, Astron. Astrophys. 445 (2006) 579–589, https://doi.org/10.1051/0004-6361:20053765.

[3] C.A. Kierans, S.E. Boggs, A. Zoglauer, A.W. Lowell, C. Sleator, J. Beechert, T.J. Brandt, P. Jean, H. Lazar, J. Roberts, T. Siegert, J.A. Tomsick, P. von Ballmoos, Detection of the 511 keV Galactic positron annihilation line with COSI, Astrophys. J. 895 (2020) 44, https://doi.org/10.3847/1538-4357/ab89a9.

[4] T. Siegert, R. Diehl, G. Khachatryan, M.G.H. Krause, F. Guglielmetti, J. Greiner, A.W. Strong, X. Zhang, Gamma-ray spectroscopy of positron annihilation in the Milky Way, Astron. Astrophys. 586 (2016) A84, https://doi.org/10.1051/0004-6361/201527510.

[5] T. Siegert, R. Diehl, J. Greiner, M.G.H. Krause, A.M. Beloborodov, M. Cadolle Bel, F. Guglielmetti, J. Rodriguez, A.W. Strong, X. Zhang, Positron annihilation signatures associated with the outburst of the microquasar V404 Cygni, Nature 531 (2016) 341–343, https://doi.org/10.1038/nature16978.

[6] J. Knoedlseder, P. Jean, V. Lonjou, G. Weidenspointner, N. Guessoum, R. Diehl, W. Gillard, M.J. Harris, G.K. Skinner, P. von Ballmoos, G. Vedrenne, P. Caraveo, B. Cordier, V. Schoenfelder, B.J. Teegarden, The all-sky distribution of 511 keV electron-positron annihilation emission, Astron. Astrophys. 441 (2005) 513–532, https://doi.org/10.1051/0004-6361:20042063.

[7] H. Yoneda, T. Siegert, S. Mittal, Imaging the positron annihilation line with 20 years of INTEGRAL/SPI observations, Astron. Astrophys. 702 (2025) A220, https://doi.org/10.1051/0004-6361/202555895.

[8] T. Siegert, S.E. Boggs, J.A. Tomsick, A.C. Zoglauer, C.A. Kierans, C.C. Sleator, J. Beechert, T.J. Brandt, P. Jean, H. Lazar, A.W. Lowell, J.M. Roberts, P. von Ballmoos, Imaging the 511 keV positron annihilation sky with COSI, Astrophys. J. 897 (2020) 45, https://doi.org/10.3847/1538-4357/ab9607.

[9] T. Siegert, R.M. Crocker, R. Diehl, M.G.H. Krause, F.H. Panther, M.M.M. Pleintinger, C. Weinberger, Constraints on positron annihilation kinematics in the inner Galaxy, Astron. Astrophys. 627 (2019) A126, https://doi.org/10.1051/0004-6361/201833856.

[10] G. De Cesare, Searching for the 511 keV annihilation line from galactic compact objects with the IBIS gamma ray telescope, Astron. Astrophys. 531 (2011) A56, https://doi.org/10.1051/0004-6361/201116516.

[11] N.M. Barriere, L. Natalucci, N. Abrosimov, P. von Ballmoos, P. Bastie, P. Courtois, M. Jentschel, J. Knodlseder, J. Rousselle, P. Ubertini, Soft gamma-ray optics: new Laue lens design and performance estimates, Proc. SPIE 7437 (2009) 74370K, https://doi.org/10.1117/12.826138.

[12] N.M. Barriere, J.A. Tomsick, S.E. Boggs, A. Lowell, P. von Ballmoos, Developing a second generation Laue lens prototype: high reflectivity crystals and accurate assembly, Proc. SPIE 8147 (2011) 81471D, https://doi.org/10.1117/12.899893.

[13] G. Weidenspointner, C.B. Wunderer, N. Barriere, A. Zoglauer, P. von Ballmoos, Monte Carlo study of detector concepts for the MAX Laue Lens gamma-ray telescope, Exp. Astron. 20 (2005) 375–386, https://doi.org/10.1007/s10686-006-9035-4.

[14] F. Shirazi, E. Gau, M.A. Hossen, D. Becker, D. Schmidt, D. Swetz, D. Bennett, D. Braun, F. Kislat, J. Gard, J. Mates, J. Weber, N.R. Cavero, S. Chun, L. Lisalda, A. West, B. Dev, F. Ferrer, R. Bose, J. Ullom, H. Krawczynski, The 511-CAM Mission: A pointed 511 keV gamma-ray telescope with a focal plane detector made of stacked transition edge sensor microcalorimeter arrays, J. Astron. Telesc. Instrum. Syst. 9 (2023) 024006, https://doi.org/10.1117/1.JATIS.9.2.024006.

[15] K. Hu, M. Fritts, D. Becker, D. Schmidt, F. Zhou, A. Dasgupta, F. Kislat, M. Keller, S. Chun, A.G. Detoito, E. Gau, X. Jin, D. Bennett, D. Braun, J. Gard, J.A.B. Mates, J. Nobles, D. Radomski, N. Rodriguez Cavero, R. Snodgrass, D. Swetz, J. Ullom, S. Vengalil Menon, J. Weber, K. Wimalasena, H. Krawczynski, Design of a mission to measure the shape and substructure of the 511 keV gamma-ray line from the center of the Milky Way, J. Astron. Telesc. Instrum. Syst. 12 (2026) 025002, https://doi.org/10.1117/1.JATIS.12.2.025002.

[16] S. Gallego, U. Oberlack, J. Lommler, C.M. Karwin, A. Zoglauer, P. Jean, P. von Ballmoos, C. Kierans, C.C. Sleator, J.A. Tomsick, S.E. Boggs, Bottom-up background simulations of the 2016 COSI balloon flight, Astrophys. J. 986 (2025) 116, https://doi.org/10.3847/1538-4357/add6a0.

[17] R. Tian, J. Mao, J. Liu, H. Jin, W. Cui, Simulation of non X-ray background for the DIffuse X-ray Explorer (DIXE) mission, Exp. Astron. 61 (2026) 17, https://doi.org/10.1007/s10686-026-10053-z.

[18] L. Gottardi, K. Nagayoshi, A review of X-ray microcalorimeters based on superconducting transition edge sensors for astrophysics and particle physics, Applied Sciences 11 (2021) 3793, https://doi.org/10.3390/app11093793.

[19] L. Xie, Y. Zhang, Z. Li, Z. Liu, S. Shu, J. Zhou, X. Li, H. Li, H. Gao, Y. Gu, X. Lu, Y. Zhao, C. Liu, Beyond one-thousandth energy resolution with an AlMn TES detector, Appl. Phys. Lett. 128 (2026) 242601, https://doi.org/10.1063/5.0326856.

[20] E.M. Vavagiakis, N.F. Cothard, J.R. Stevens, C.L. Chang, M.D. Niemack, G. Wang, V.G. Yefremenko, J. Zhang, Developing AlMn films for Argonne TES fabrication, J. Low Temp. Phys. 199 (2020) 408–415, https://doi.org/10.1007/s10909-019-02281-9.

[21] E.M. Vavagiakis, S.W. Henderson, K. Zheng, H.-M. Cho, N.F. Cothard, B. Dober, S.M. Duff, P.A. Gallardo, G. Hilton, J. Hubmayr, K.D. Irwin, B.J. Koopman, D. Li, F. Nati, M.D. Niemack, C.D. Reintsema, S. Simon, J.R. Stevens, A. Suzuki, B. Westbrook, Magnetic sensitivity of AlMn TESes and shielding considerations for next-generation CMB surveys, J. Low Temp. Phys. 193 (2018) 288–297, https://doi.org/10.1007/s10909-018-1920-5.

[22] M.J. Berger, J.H. Hubbell, S.M. Seltzer, J. Chang, J.S. Coursey, R. Sukumar, D.S. Zucker, K. Olsen, XCOM: Photon Cross Sections Database, NIST Standard Reference Database 8 (XGAM), data updated November 2010, National Institute of Standards and Technology, https://doi.org/10.18434/T48G6X. https://www.nist.gov/pml/xcom-photon-cross-sections-database (accessed 21 September 2026).

[23] D. Yan, L.M. Gades, T. Guruswamy, U.M. Patel, O. Quaranta, A. Miceli, Modelling a transition-edge sensor X-ray microcalorimeter linear array for Compton profile measurements and energy dispersive diffraction, IEEE Trans. Appl. Supercond. 29(5) (2019) 1–4, https://doi.org/10.1109/TASC.2019.2906255.

[24] A. Zoglauer, R. Andritschke, F. Schopper, MEGAlib: The Medium Energy Gamma-ray Astronomy Library, New Astron. Rev. 50 (2006) 629–632, https://doi.org/10.1016/j.newar.2006.06.049.

[25] S. Agostinelli, J. Allison, K. Amako, et al., Geant4—a simulation toolkit, Nucl. Instrum. Methods Phys. Res. A 506 (2003) 250–303, https://doi.org/10.1016/S0168-9002(03)01368-8.

[26] J. Allison, K. Amako, J. Apostolakis, et al., Recent developments in Geant4, Nucl. Instrum. Methods Phys. Res. A 835 (2016) 186–225, https://doi.org/10.1016/j.nima.2016.06.125.

[27] N. Barrière, J. Rousselle, P. von Ballmoos, et al., Experimental and theoretical study of the diffraction properties of various crystals for the realization of a soft gamma-ray Laue lens, J. Appl. Crystallogr. 42 (2009) 834–845, https://doi.org/10.1107/S0021889809023218.

[28] M. Sanchez del Rio, R.J. Dejus, XOP v2.4: recent developments of the x-ray optics software toolkit, Proc. SPIE 8141 (2011) 814115, https://doi.org/10.1117/12.893911.

[29] T. Schoonjans, A. Brunetti, B. Golosio, M. Sanchez del Rio, V.A. Solé, C. Ferrero, L. Vincze, The xraylib library for X-ray–matter interactions. Recent developments, Spectrochim. Acta B 66 (2011) 776–784, https://doi.org/10.1016/j.sab.2011.09.011.

[30] F. Bornemann, Y. Y. Li, J. Wuttke, Multiple Bragg reflection by a thick mosaic crystal. II. Simplified transport equation solved on a grid, Acta Crystallogr. A76 (2020) 376–389, https://doi.org/10.1107/S2053273320002065.

[31] T. Sato, Analytical model for estimating terrestrial cosmic ray fluxes nearly anytime and anywhere in the world: extension of PARMA/EXPACS, PLoS ONE 10 (2015) e0144679, https://doi.org/10.1371/journal.pone.0144679.

[32] T. Sato, Analytical model for estimating the zenith angle dependence of terrestrial cosmic ray fluxes, PLoS ONE 11 (2016) e0160390, https://doi.org/10.1371/journal.pone.0160390.

[33] P. Cumani, M. Hernanz, J. Kiener, V. Tatischeff, A. Zoglauer, Background for a gamma-ray satellite on a low-Earth orbit, Exp. Astron. 47 (2019) 273–302, https://doi.org/10.1007/s10686-019-09624-0.

[34] F.G. Kondev, M. Wang, W.J. Huang, S. Naimi, G. Audi, The NUBASE2020 evaluation of nuclear physics properties, Chinese Phys. C 45 (2021) 030001, https://doi.org/10.1088/1674-1137/abddae.

[35] C.A. Kierans, S.E. Boggs, J.-L. Chiu, A. Lowell, C. Sleator, J.A. Tomsick, A. Zoglauer, M. Amman, H.-K. Chang, C.-H. Tseng, C.-Y. Yang, C.-H. Lin, P. Jean, P. von Ballmoos, The 2016 Super Pressure Balloon flight of the Compton Spectrometer and Imager, PoS INTEGRAL2016 (2017) 075, https://doi.org/10.22323/1.285.0075.

[36] G. Cowan, K. Cranmer, E. Gross, O. Vitells, Asymptotic formulae for likelihood-based tests of new physics, Eur. Phys. J. C 71 (2011) 1554, https://doi.org/10.1140/epjc/s10052-011-1554-0.

[37] T. Takahashi et al., Hard X-Ray Detector (HXD) on Board Suzaku, Publ. Astron. Soc. Jpn. 59 (2007) S35–S51, https://doi.org/10.1093/pasj/59.sp1.S35.

[38] M.-A. Verdier, P.C.F. Di Stefano, P. Nadeau, C. Behan, M. Clavel, C. Dujardin, Scintillation properties of $Bi_4Ge_3O_{12}$ down to 3 K under γ rays, Phys. Rev. B 84 (2011) 214306, https://doi.org/10.1103/PhysRevB.84.214306.

[39] J. van der Kuur et al., The SPICA-SAFARI TES Bolometer Readout: Developments Towards a Flight System, J. Low Temp. Phys. 167 (2012) 561–567, https://doi.org/10.1007/s10909-012-0521-y.

[40] M.I. Dobynde, J. Guo, Radiation environment at the surface and subsurface of the Moon: model development and validation, J. Geophys. Res. Planets 126 (2021) e2021JE006930, https://doi.org/10.1029/2021JE006930.

[41] S. Lotti et al., Review of the particle background of the Athena X-IFU instrument, Astrophys. J. 909 (2021) 111, https://doi.org/10.3847/1538-4357/abd94c.

[42] I.G. Usoskin, K. Alanko-Huotari, G.A. Kovaltsov, K. Mursula, Heliospheric modulation of cosmic rays: monthly reconstruction for 1951–2004, J. Geophys. Res. Space Phys. 110 (2005) A12108, https://doi.org/10.1029/2005JA011250.

[43] N.V. Kuznetsov, H. Popova, M.I. Panasyuk, Empirical model of long-time variations of galactic cosmic ray particle fluxes, J. Geophys. Res. Space Phys. 122 (2017) 1463–1472, https://doi.org/10.1002/2016JA022920.

[44] R. Agnese et al., Nuclear-recoil energy scale in CDMS II silicon dark-matter detectors, Nucl. Instrum. Methods Phys. Res. A 905 (2018) 71–81, https://doi.org/10.1016/j.nima.2018.07.028.

[45] S.V. Hull et al., Characterizing thermal background events for Athena X-IFU, IEEE Trans. Appl. Supercond. 33 (2023) 2100606, https://doi.org/10.1109/TASC.2023.3257131.